Alfvénic thermospheric upwelling in a global geospace model

Benjamin Hogan[1], William Lotko[2], and Kevin Pham[3]

[1]ThayerSchool of Engineering, Dartmouth College, Hanover, NH, USA and High Altitude Observatory, National Center for Atmospheric Research, Boulder, CO, USA Now at University of Colorado Boulder Laboratory for Atmospheric and Space Physics, Boulder, CO USA
[2]High Altitude Observatory, National Center for Atmospheric Research, Boulder, CO, USA and Thayer School of Engineering, Dartmouth College, Hanover, NH, USA
[3]High Altitude Observatory, National Center for Atmospheric Research, Boulder, CO, USA

November 23, 2022

Abstract

Motivated by low-altitude cusp observations of small-scale (~ 1 km) field-aligned currents (SSFACs) interpreted as ionospheric Alfvén resonator modes, we have investigated the effects of Alfvén wave energy deposition on thermospheric upwelling and the formation of air density enhancements in and near the cusp. Such density enhancements were commonly observed near 400 km altitude by the CHAMP satellite. They are not predicted by empirical thermo-sphere models, and they are well-correlated with the observed SSFACs. A parameterized model for the altitude dependence of the Alfvén wave electric field, constrained by CHAMP data, has been developed and embedded in the Joule heating module of the National Center for Atmospheric Research (NCAR) Coupled Magnetosphere-Ionosphere-Thermosphere (CMIT) model. The CMIT model was then used to simulate the geospace response to an interplanetary stream interaction region (SIR) that swept past Earth on 26-27 March 2003. CMIT diagnostics for the thermospheric mass density at 400 km altitude show: 1) CMIT without Alfvénic Joule heating usually underestimates CHAMP's orbit-average density; inclusion of Alfvénic heating modestly improves CMIT's orbit-average prediction of the density (by a few %), especially during the more active periods of the SIR event. 2) The improvement in CMIT's instantaneous density prediction with Alfvénic heating included is more significant (up to 15%) in the vicinity of the cusp heating region, a feature that the MSIS empirical thermosphere model misses for this event. Thermospheric density changes of 20-30 % caused by the cusp-region Alfvénic heating sporadically populate the polar region through the action of co-rotation and neutral winds.

1 # Alfvénic thermospheric upwelling in a global geospace model

2 **Benjamin Hogan[1,2,†], William Lotko[1,2] and Kevin Pham[2]**

3 [1]Thayer School of Engineering, Dartmouth College, Hanover, NH, USA

4 [2]High Altitude Observatory, National Center for Atmospheric Research, Boulder, CO, USA

5 Corresponding author: Benjamin Hogan (ben.hogan@lasp.colorado.edu)

6 [†]Now at Laboratory for Atmospheric and Space Physics, University of Colorado Boulder, Boul-

7 der, CO, USA, and Department of Aerospace Sciences, University of Colorado Boulder, Boul-

8 der, CO, USA.

9

10 **Key Points:**

11 - A parameterized model for Alfvén wave heating of the thermosphere was implemented in

12   a global ionosphere-thermosphere model

13 - Alfvén wave heating increases air density in the model by 20-30% in and near the cusp at

14   CHAMP altitudes ($\approx$413 km) during an SIR event

15 - Heating effects are not localized to the cusp during the event and improve model accura-

16   cy compared to orbit-averaged CHAMP-derived density

17

18   **Abstract**

19   Motivated by low-altitude cusp observations of small-scale (~ 1 km) field-aligned currents

20   (SSFACs) interpreted as ionospheric Alfvén resonator modes, we have investigated the effects of

21   Alfvén wave energy deposition on thermospheric upwelling and the formation of air density en-

22   hancements in and near the cusp. Such density enhancements were commonly observed near 400

23   km altitude by the CHAMP satellite. They are not predicted by empirical thermosphere models,

24   and they are well-correlated with the observed SSFACs. A parameterized model for the altitude

25   dependence of the Alfvén wave electric field, constrained by CHAMP data, has been developed

26   and embedded in the Joule heating module of the National Center for Atmospheric Research

27   (NCAR) Coupled Magnetosphere-Ionosphere-Thermosphere (CMIT) model. The CMIT model

28   was then used to simulate the geospace response to an interplanetary stream interaction region

29   (SIR) that swept past Earth on 26-27 March 2003. CMIT diagnostics for the thermospheric mass

30   density at 400 km altitude show: 1) CMIT without Alfvénic Joule heating usually underestimates

31   CHAMP's *orbit-average* density; inclusion of Alfvénic heating modestly improves CMIT's or-

32   bit-average prediction of the density (by a few %), especially during the more active periods of

33   the SIR event. 2) The improvement in CMIT's *instantaneous* density prediction with Alfvénic

34   heating included is more significant (up to 15%) in the vicinity of the cusp heating region, a fea-

35   ture that the MSIS empirical thermosphere model misses for this event. Thermospheric density

36   changes of 20-30 % caused by the cusp-region Alfvénic heating sporadically populate the polar

37   region through the action of co-rotation and neutral winds.

1. Introduction

Thermospheric density anomalies with average values 20-30% larger than empirical

model predictions are encountered by satellites orbiting near 400 km altitude in the high-latitude

dayside thermosphere (Liu et al., 2005, Rentz & Lühr et al., 2008). About 40% of CHAMP satel-

lite orbits exhibit such anomalies (Kervalishvili & Lühr, 2014). Soft electron precipitation, also

referred to as broadband precipitation with energies of 100s eV (Živković et al, 2015), and in-

tense, small-scale field-aligned currents (SSFACs) (Lühr, et al, 2004; Kervalishivli & Luhr,

2013) are well correlated with the anomalies in the cusp region. Enhanced Joule heating by qua-

sistatic electric fields may contribute to the thermospheric upwelling that produces density

anomalies, but observations (Schlegel et al., 2005) and models (Zhang et al., 2012; Deng et al.,

2013) indicate that this mechanism alone is insufficient.

Simulation studies of the thermosphere (Brinkman et al., 2016), the coupled ionosphere-

thermosphere (IT) (Deng et al, 2013) and the coupled magnetosphere-ionosphere-thermosphere

(MIT) (Zhang et al., 2012, 2015a) show that soft electron precipitation in the cusp, combined

with sufficiently intense, quasistatic electric fields, can produce density anomalies resembling

those observed in the cusp region. In all of these studies, the soft electron precipitation augments

the *F*-region Pedersen conductivity and the specific Joule heating rate at altitudes where the am-

bient air density is exponentially decreasing. The added heat and attendant increase in thermo-

spheric temperature is effective in producing upwelling and a major density perturbation of the

neutral gas (Jee et al., 2008; Clemmons et al., 2008; Brinkman et al., 2016).

Lotko and Zhang (2018) showed that the Joule heating rate resulting from persistent and

more or less continuously driven, small-scale Alfvénic perturbations representative of the

SSFACs regularly observed by CHAMP in the cusp can be significant at *F*-region altitudes (200-

61   400 km). Transient Alfvénic perturbations accompanying discontinuities in solar wind driving

62   are also expected to augment *F*-region Joule heating (Tu et al., 2011) and contribute to enhance-

63   ments in thermospheric density at these altitudes, but isolated transients in Alfvénic energy depo-

64   sition cannot account for the relatively high probability of observing a thermospheric density

65   anomaly on any given satellite pass through the cusp. In contrast with quasistatic electric fields,

66   which are practically independent of altitude in the thermosphere, Alfvénic electric fields are

67   more intense in the *F*-region than in the *E*-region owing to the influence of the ionospheric Alf-

68   vén resonator (IAR). The IAR traps Alfvén waves and intensifies their amplitudes near the *F*-

69   region peak in plasma density where the wave speed is slow (Trakhtengerts & Fel'Dshtein, 1984;

70   Lysak, 1991). The results suggest that Alfvén wave energy deposition in the IAR may contribute

71   to air density anomalies at CHAMP altitudes in the absence of Joule heating by intense quasistat-

72   ic electric fields.

73   The SSFACs recorded by CHAMP in association with density anomalies have been in-

74   terpreted as IAR modes (Rother et al., 2007). However, distinguishing Alfvén waves with char-

75   acteristic wave impedance and phase relations (e.g., Ishii et al., 1992) from quasistatic variability

76   requires simultaneous electric and magnetic field measurements. CHAMP carried a sensitive

77   magnetometer but no electric field sensor. Measurements from the Polar (Keiling et al., 2003)

78   and FAST (Chaston et al., 2007; Hatch et al., 2017) satellites have been used to definitively iden-

79   tify Alfvénic fluctuations and their distributions in magnetic local time (MLT) and magnetic lati-

80   tude (MLAT). The statistical distribution of the most probable occurrence of Alfvénic fluctua-

81   tions from FAST shown in Figure 1 (lower right) correlate well with the MLT-MLAT distribu-

82   tion of CHAMP thermospheric density anomalies (Fig. 1, upper left), as does the distribution of

83   soft electron precipitation derived from DMSP satellite measurements (Fig. 1, upper right).
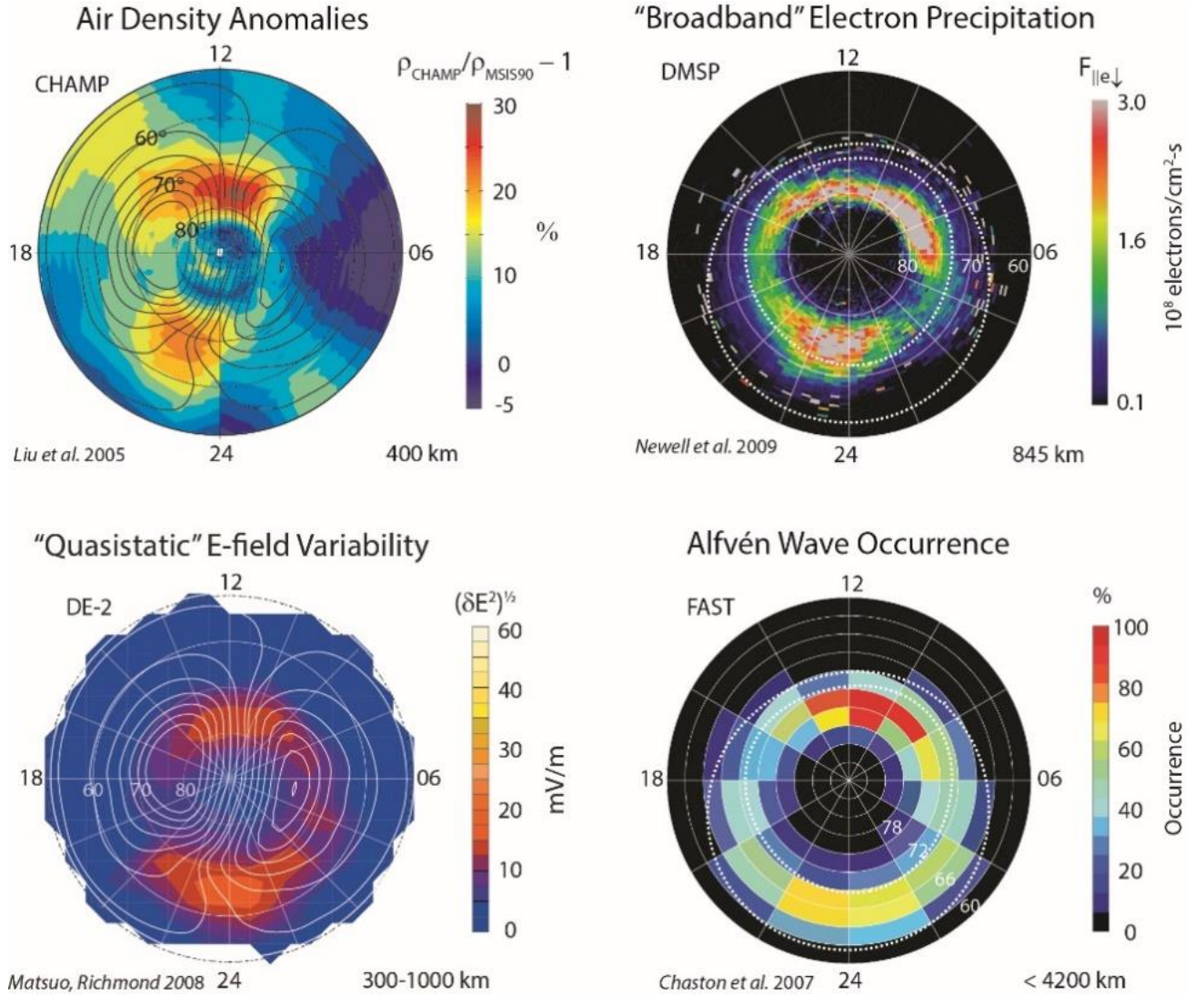
Figure 1. Top left: One-year average difference between air density recorded by CHAMP in the northern hemisphere and estimated from MSIS. Illustrative CMIT convection streamlines superposed. Top right: Statistical number flux of broadband electron precipitation from DMSP. Feldstein statistical auroral oval superposed as dotted lines. Bottom left: Statistical root-mean-square electric field variability from DE-2, with same illustrative convection lines. Bottom right: Occurrence of Alfvén waves recorded by FAST, also with Feldstein oval superposed. All figures are in MLT-MLAT (magnetic local time, magnetic latitude) coordinates. Source of plot and nominal altitude of measurements are indicated at the bottom of each.

84

85   The MLT-MLAT distribution of quasistatic electric field variability is also shown in Fig. 1 (low-

86   er left) because it has been posited as a possible causal agent for the enhanced Joule heating

87   needed to produce the CHAMP density anomalies (Deng et al., 2013; Brinkman et al., 2016).

88   This particular distribution derived by Matsuo & Richmond (2008) from DE-2 satellite data for

89   summer conditions and clock angles of 45°-135° of the interplanetary magnetic field (IMF) also

90   resembles the distribution of CHAMP anomalies. Distributions of electric field variability for

91   winter and equinox conditions and other IMF clock angles are very different and, for some con-

92   ditions (e.g., summer and IMF clock angles between 135°-225) exhibit very low amplitudes

93   where CHAMP anomalies occur. Matsuo & Richmond's distributions of electric field variability

94   assume the observed variation is spatial (no time variation) with contributions integrated over

95   horizontal scales between 3 km and 500 km. The assumption of static electric field variability

96   may limit the applicability of these results, particularly for contributions at the smaller scales (<

97   few 100 km), for which Alfvénic rather than quasistatic variability is usually prominent (Ishii et

98   al., 1992; Chaston et al., 2003; Lühr et al., 2015; Park et al., 2017).

99   We focus in this paper on the effects of Alfvén wave energy deposition on the thermo-

100   spheric mass density in and near the low-altitude cusp at the nominal CHAMP altitude of 400

101   km. The Alfvén wave model of Lotko & Zhang (2018) is adapted as a parameterized model in

102   the NCAR Coupled Magnetosphere-Ionosphere model (CMIT), which is used to simulate and

103   analyze the MIT response to the stream interaction region (SIR) that swept past Earth on 26-27

104   March 2003. The relative importance of Alfvénic Joule heating for this event is characterized as

105   a difference in thermospheric mass densities at 400 km altitude with and without inclusion of

106   Alfvénic heating. The CMIT model includes i) a cusp-finding algorithm (Zhang et al., 2013),

107   which dynamically determines where the Alfvénic Joule heating is to be applied, and ii) a causal-

108   ly regulated empirical specification for soft electron precipitation. The soft precipitation is mod-

109   eled as both direct-entry cusp precipitation and Alfvén wave-induced "broadband" precipitation

110   (Zhang et al., 2015b). As mentioned above, soft precipitation and some type of electric field en-

111   hancement are important factors in producing thermospheric density enhancement in the cusp

112   region.

113   We first provide an overview of the CMIT model and the interplanetary conditions for

114   the SIR event to be simulated (Section 2.1). The parameterized Alfvén wave model to be embed-

115   ded in CMIT is described (Section 2.2), along with specification of the ambient IT parameters

116   that determine the characteristics of Alfvén propagation and absorption (Section 2.3) and integra-

117   tion of the Alfvén wave heating model into CMIT (Section 2.4). Discussion of the simulation

118   results (Section 3) and principal conclusions (Section 4) follow.

119

120   **2. Methods**

121   **2.1 Overview of CMIT and the 26-27 March 2003 SIR event**

122   NCAR's CMIT model has been used previously to simulate the MIT response to solar

123   wind and interplanetary driving (Wang et al., 2004; Wiltberger et al., 2004; Zhang et al., 2012,

124   2015a, Liu et al., 2018). The magnetospheric component of CMIT is the Lyon-Fedder-Mobarry

125   (LFM) global magnetosphere simulation model, which describes the coupling between the solar

126   wind and magnetosphere by solving the three-dimensional equations of ideal magnetohydrody-

127   namics (Lyon et al., 2004). The so-called "double-resolution" version (53x48x64 grid cells) of

128   LFM is used here. Its physical domain is a distorted spherical grid extending 30 Earth radii (R_E)

129   upstream from Earth into the solar wind, to 300 R_E downstream on the nightside, and 100 R_E on

130   the sides. The LFM model is driven by time series of state variables for the solar wind and IMF

131   obtained from interplanetary satellite measurements (the one-minute OMNI-combined data

132   available at https://cdaweb.gsfc.nasa.gov/index.html/).

133   The ionosphere and thermosphere (IT) component of CMIT is modeled by the Thermo-

134 sphere-Ionosphere Electrodynamics General Circulation Model (TIEGCM), which solves the

135 three-dimensional equations of continuity, momentum and energy for neutral and ion gases of

136 the IT system. The TIEGCM version used here determines state variables globally on a uniform

137 geographic grid of 1.25° in both latitude and longitude with 57 pressure levels at different alti-

138 tudes (Dang et al., 2018; Qian et al., 2013; Wang et al., 2008). In addition to its inputs from LFM

139 – convection velocity and electron precipitation flux and energy – TIEGCM uses the F10.7 index

140 for solar radio flux to parameterize its extreme ultraviolet ionization.

141   The MIX solver couples TIEGCM and LFM on a uniform grid of 2° in MLAT and mag-

142 netic longitude and extends from the poles down to 46° MLAT. MIX takes conductance infor-

143 mation from TIEGCM and the field-aligned current (FAC) distribution from LFM to solve a

144 Poisson equation for the electric potential at the ionospheric height. The potential determines the

145 ionospheric convection velocity in TIEGCM and a velocity boundary condition at LFM's low-

146 altitude boundary after mapping it along equipotential, magnetic dipole field lines to the bounda-

147 ry (Merkin & Lyon 2010). The time interval between LFM-MIX-TIEGCM data exchanges is 5 s.

148 TIEGCM's time step is set to be the same as the (5 s) exchange time.

149   The low-altitude cusp finding algorithm developed by Zhang et al. (2013) from LFM

150 state variables is used to define the cusp area. This simulated dynamic cusp is projected onto

151 TIEGCM's grid where low-energy, direct-entry cusp electron precipitation is specified, also us-

152 ing LFM state variables. Direct-entry cusp precipitation is distinct from broadband, monoener-

153 getic and diffuse precipitation which MIX also determines from LFM state variables and passes

154 to TIEGCM (Zhang et al., 2015b). Low-energy electron cusp precipitation has been shown to be

155 important in thermospheric heating in the cusp because it enhances the bottomside *F*-region

156 Pedersen conductivity and thermospheric heating there (Clemmons et al., 2008; Zhang et al.,
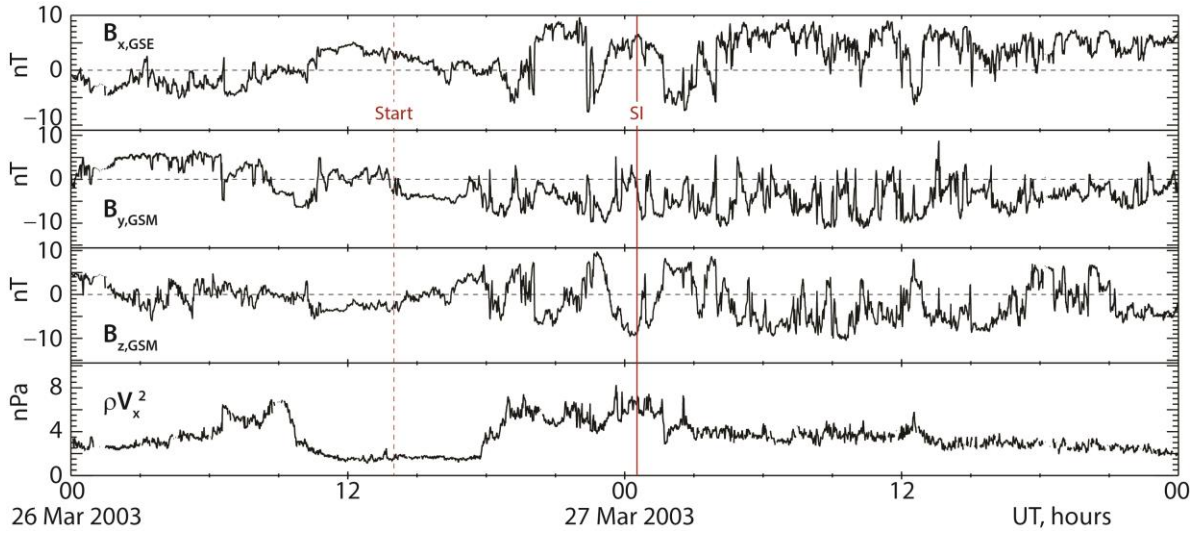
Figure 2. IMF and solar wind dynamic pressure from 00 UT on 26 March 2003 through 00 UT on 28 March 2003. The red dashed and solid vertical lines respectively mark the start of the SIR event at 1400 UT and its stream interface at 0038 UT (Jian et al., 2006), neither of which delineates a distinct transition in the plotted variables.

157   2012, 2015a; Deng et al., 2013; Brinkman et al., 2016). We use LFM's cusp finding algorithm to

158   specify the TIEGCM cells in which Alfvénic heating is imposed (Section 2.4).

159   We used CMIT to investigate the thermospheric heating and upwelling that occurred as a

160   stream interaction region (SIR) swept past Earth on 26-27 March 2003 (Figure 2). We chose an

161   SIR event because variability in the solar wind and IMF accompanying such events is expected

162   to produce intense Alfvénic activity in the cusp. During this event the CHAMP mean altitude

163   (413 km) is comparable to the altitude where the distribution of density anomalies in Fig. 1 occur

164   (Liu et al., 2005). Hemispheric asymmetries in the ionospheric conductivities are minimized

165   (though not entirely absent) because the event is near spring equinox. No SIRs occurred in the 11

166   days prior to this event (Jian et al., 2006), so a less disturbed MIT system is expected at model

167   start time, making the geospace response to the SIR reasonably distinct. The sampled IT envi-

168   ronment begins to respond to the SIR around 00:00 UT on the 27th (described in Section 3) which

169   is the middle of the simulated period. The first day of the event (until 1800 UT) exhibits weak-

170   to-moderate activity in the IMF; the second day exhibits more intense and persistent variability

171   in the IMF.

172   Using IMF data to drive LFM requires special treatment of a variable IMF B_x in order to

173   maintain $\nabla \cdot \mathbf{B} = 0$ in the interplanetary medium (Lyon et al., 2004). As described in Text S1 of

174   the Supporting Information, we used the method of Wiltberger et al. (2000) to specify the varia-

175   ble IMF B_x for this event. To reduce memory of initial conditions in simulating the SIR event,

176   TIEGCM and LFM were separately preconditioned as described in Text S2 of the Supporting

177   Information.

178

2.2 Parameterized Alfvén wave model

180   We consider energy deposition in the cusp ionosphere by low-frequency magnetohydro-

181   dynamic waves, presumed to be generated at high altitudes near the magnetopause by interplane-

182   tary variability and/or magnetopause dynamics associated with dayside reconnection and Kelvin-

183   Helmholtz surface waves. In general, such disturbances stimulate slow and fast mode compres-

184   sional waves and intermediate mode shear Alfvén waves. Slow mode waves encounter strong ion

185   Landau damping in the magnetosphere where the ion to electron temperature ratio typically ex-

186   ceeds one. Consequently, very little slow mode power stimulated by high-altitude disturbances

187   reaches the ionosphere. The group velocity of fast mode waves is nearly isotropic, so fast mode

188   power falls off as r^{-2} with distance r from the source. The power carried by nondispersive, shear

189   Alfvén waves reaches the ionosphere most efficiently because (nondispersive) shear Alfvén

190   waves are guided practically loss-free along magnetic field lines, and their energy is magnetical-

191   ly focused by the converging flux tube. The field-aligned Poynting flux $S_{\parallel}$ of the Alfvén wave

192   varies approximately with magnetic field intensity B as $S_{\parallel}/B$. For these reasons, we consider en-

193   ergy deposition resulting only from shear mode Alfvén waves and neglect signals and ionospher-

194   ic energy deposition resulting from slow and fast mode waves.

195   The linear model for collisional propagation and absorption of Alfvén waves in the iono-

196   sphere-thermosphere used in this study is described by Lotko & Zhang (2018). It neglects mag-

197   netic compressibility, ionospheric Hall currents and electron inertia, which, as discussed by Lot-

198   ko and Zhang, is appropriate for angular wave frequencies ($\omega = 2\pi f$) and perpendicular wave-

199   numbers $k_\perp$ satisfying $\mu_0 e^2 n_e / m_e \gg k_\perp^2 \gg \mu_0 \omega \sigma_H^2 / \sigma_P$ for given Hall (σ_H) and Pedersen (σ_P)

200   conductivities, the permeability of free space (μ_0), and the electron charge (e), mass (m_e) and

201   density (n_e). We also neglect the effects of neutral-gas inertia, mediated by ion-neutral friction,

202   on Alfvén wave propagation and dissipation. These effects are negligible when $\omega \gg \nu_i \, \rho_i / \rho_n$

203   where ρ_i and ρ_n are the ion and neutral mass densities and ν_i is the ion-neutral collision frequen-

204   cy (see Supporting Information Text S3 and Figure S2).

205   The equations of Lotko & Zhang (2018) are:

$$\partial_t \mathbf{E}_\perp + \nu_P \mathbf{E}_\perp = V^2 \left(\nabla \times \mathbf{B} \right)_\perp , \tag{1}$$

$$\partial_t \mathbf{B} = -\left(\nabla \times \mathbf{E} \right) , \tag{2}$$

$$E_\parallel = j_\parallel / \sigma_0 = \eta \, \hat{\mathbf{b}} \cdot \left(\nabla \times \mathbf{B} \right) . \tag{3}$$

209    $\mathbf{E}_\perp$ and $\mathbf{B}_\perp$ are the wave perpendicular electric and magnetic fields; $j_\parallel$ is the wave field-aligned

210   current derived from $\mathbf{B}_\perp$; $\hat{\mathbf{b}}$ is the unit vector in the local magnetic-field direction. In (1) and (3)

211   the Pedersen dissipation rate ($\nu_P = \sigma_P / \varepsilon$) and magnetic diffusivity ($\eta = 1/\sigma_0 \mu_0$) are given in

212   terms of the Pedersen and direct or parallel (σ_0) conductivities as

$$\sigma_P = \sum_s \frac{n_s q_s^2}{m_s} \frac{\nu_s}{\nu_s^2 + \Omega_s^2} , \tag{4}$$

214
$$\sigma_0 = \frac{n_e e^2}{m_e \nu_e}. \tag{5}$$

215 The wave speed ($V = 1/(\mu_0 \varepsilon)^{1/2} = c(\varepsilon_0/\varepsilon)^{1/2}$) in (2) depends on the speed of light in vacuum

216 (c), the vacuum permittivity (ε_0) and the dielectric constant (ε) for Alfvén wave propagation in-

217 cluding collisional effects

218
$$\varepsilon = \varepsilon_0 \left(1 + \sum_s \frac{\omega_{ps}^2}{\nu_s^2 + \Omega_s^2}\right). \tag{6}$$

219 Plasma parameters in (4)-(6) include the number density (n_s), charge (q_s), mass (m_s), plasma

220 frequency (ω_{ps}) and collision frequency (ν_s) of charged-particle species s (*e* for electrons, *i* for

221 ion species). The collision frequencies are taken from Schunk & Nagy (SN) (2009). For ions, ν_s

222 includes ion-neutral collisions (SN, equation 4.146 and Table 4.4; Table 4.5); for electrons, it

223 includes electron-ion (SN, equation 4.144) and electron-neutral collisions (SN, Table 4.6).

224 Our focus is on low-altitude collisional Alfvénic energy deposition (below 1000 km and

225 mostly below 500 km), so we follow the method of Lotko & Zhang (2018) and simplify the

226 analysis by treating the geomagnetic field as straight and uniform. The implications and accom-

227 modations of this treatment are described in Text S4 of the Supporting Information.

228 At this juncture we neglect spatial gradients in MLT in the background parameters and in

229 Alfvén waveforms, which is also assumed in deducing SSFACs from low-altitude satellite data

230 (see below). The 2D form of (1)-(3) in coordinates parallel (z) and perpendicular (x) to the back-

231 ground magnetic field (x corresponds to the magnetic meridional or MLAT direction, positive

232 toward north) become, after combining (2) and (3),

233
$$\left(\frac{\partial}{\partial t} + \nu_P\right) E_x = -V^2 \frac{\partial B_y}{\partial z}, \tag{7}$$

12

234
$$\frac{\partial B_y}{\partial t} = -\frac{\partial E_x}{\partial z} + \frac{\partial}{\partial x}\left(\eta\frac{\partial B_y}{\partial x}\right).$$
(8)

235   We neglect perpendicular (MLAT) spatial variations in background parameters ν_P, V and

236 η, which is valid when the length scales for such spatial variations are large compared to the per-

237 pendicular wavelength. Equations (7) and (8) are solved by harmonic solutions of the form

238
$$E_x(x,z,t) = \sum_{m=1}^{M}\sum_{n=1}^{N} E_{m,n}(z)\cos\left(k_m x + \theta_m\right)\cos\left(\omega_n t + \theta_n\right),$$
(9)

239
$$B_y(x,z,t) = \sum_{m=1}^{M}\sum_{n=1}^{N} B_{m,n}(z)\cos\left(k_m x + \theta_m\right)\cos\left(\omega_n t + \theta_n + \phi_{m,n}\right).$$
(10)

240 $E_{m,n}(z)$ and $B_{m,n}(z)$ are altitude-dependent Fourier amplitudes; $\phi_{m,n}(z)$ is the altitude-

241 dependent phase difference between the wave electric and magnetic field for each mode;

242 $k_m = 2\pi m/\lambda_{\max}$ is the wavenumber; $\omega_n = 2\pi n/\tau_{\max}$ is the angular frequency; and $\lambda_{\max}$ and

243 $\tau_{\max}$ are the maximum meridional perpendicular wavelength (100 km) and wave period (20 sec)

244 considered. Lacking knowledge of any correlations or relationships between the different modes,

245 we assume they are uncorrelated with random phases θ_m and θ_n on the interval $[0, 2\pi]$.

246   The expansions include $M \times N = 400 \times 40$ modes. The following considerations were

247 made in choosing the upper and lower cutoffs on perpendicular wavenumbers and frequencies.

248   – Modes with perpendicular wavelengths $\lesssim 2$ km encounter strong Ohmic dissipation in

249   the topside ionosphere (Lotko & Zhang, 2018), mainly due to electron-ion collisions.

250   Ohmic dissipation heats electrons, with very little thermospheric heating. The expansions

251   (9) and (10) include wavelengths as short as $\lambda_{\max}/M = 250$ m, but thermospheric heat-

252   ing and upwelling are relatively insensitive to inclusion of these short wavelength modes.

253   – The longest wavelength included in (9) and (10) ($\lambda_{\max} = 100$ km) is an appropriate up-

254   per limit on the wavelength spectrum when modeling parameterized Alfvénic heating in

255   CMIT when the TIEGCM cell size is 1.25° (140 km) and the MIX and LFM cell sizes are

256   220 km or larger when referenced to 100 km altitude.

257   –   Alfvén waves with frequencies comparable to or greater than the local proton gyrofre-

258   quency near the magnetopause are locally absorbed by ion-cyclotron resonant interac-

259   tions (Stawarz et al., 2016). For this reason, we do not include modes with frequencies

260      $> N/\tau_{\max} = 2$ Hz in (9) and (10) because they do not propagate from the near-

261   magnetopause region to the low-altitude region of interest.

262   –   The lowest frequency mode ($f_{\min} = 1/\tau_{\max}$) in (9) and (10) is practically quasi-static.

263   Including electric field variability with frequencies below $f_{\min}$ would augment the dc

264   Joule heating rate in CMIT, which is treated in the Joule heating module of TIEGCM, as

265   discussed in Section 2.4.

266   In solving (7) and (8), the harmonic dependence in x is first introduced which converts

267 $\partial^2/\partial x^2$ in (8) to $-k_m^2$. The altitude dependent amplitudes $E_{m,n}(z)$ and $B_{m,n}(z)$ and phases

268 $\phi_{m,n}(z)$, now parameterized by k_m, are then derived from the finite-difference time-domain

269 (FDTD) numerical method described by Christ et al. (2002) with modes stimulated by a time-

270 periodic driver with frequency $n/\tau_{\max}$ at altitude $z = 4500$ km and electric field amplitude

271 $E_{m,n}(z_d)$. Setting $B_{m,n}(z_d) = E_{m,n}(z_d)/V(z_d)$ at the driver stimulates a downward propagating

272 Alfvén wave. The computational domain extends from the Earth's surface ($z = 0$ km altitude) up

273 to $z = 5000$ km. The FDTD solver with Mur absorbing boundary conditions (Mur, 1981) is run

274 until its solution converges to the harmonic forms (9) and (10) (Lotko & Zhang, 2018).

275   We impose observational constraints on the FDTD solution by adjusting (through trial and

276 error) the frequency and wavenumber dependence of $E_{m,n}(z_d)$ to produce an amplitude-

277 frequency spectrum for the field-aligned current (FAC) similar to the average spectrum shown in

278   Figure 3 of Rother et al. (2007), derived from CHAMP satellite measurements at an altitude of

279   approximately 400 km. The procedure for imposing the constraints is as follows.

280   –   As is typical when determining the FAC from satellite measurements of the magnetic

281   field (Lühr et al., 1996), Rother et al. assume (i) the FAC is effectively sheet-like (also

282   consistent with the 2D approximation used in (7) and (8)) and (ii) the curl of the magnetic

283   field is equivalent to the along-track Doppler derivative normal to the sheet, i.e., $\partial/\partial x =$

284         $\partial/V_s\partial t$. Here, x is the spatial coordinate normal to the sheet and the background magnet-

285   ic field. $V_s \approx 7.6$ km/s is the component of the CHAMP satellite velocity normal to the

286   sheet and the background magnetic field. The extent to which these observational as-

287   sumptions are valid for the events reported by Rother et al. (2007) is not clear, but we

288   simulate the procedure as follows:

289   –   In (10), we set $x = V_s t$, differentiate the resulting expansion with respect to $V_s t$, and di-

290   vide the result by μ_0 to obtain the simulated, Doppler-derived FAC as a function of time.

291   –   Sample time series of the Doppler-derived FAC along a simulated CHAMP satellite track

292   may then be constructed and its Fast Fourier Transform calculated to obtain a sample

293   amplitude-frequency spectrum. Choosing the n and m dependence of the modal ampli-

294   tudes at the driver to be

$$E_{m,n}\left(z_d\right) = \frac{E_0}{n\sqrt{n^2 + 2.4m^2}} \tag{11}$$

296   was found to approximate the spectral shape of the FACs reported by Rother et al.

297   (2007). E_0= 500 mV/m produced a peak FAC in the Doppler-derived time series compa-

298   rable to the mean peak value of 350 $\mu A/m^2$ in Fig. 7 of Rother et al. (2007). The ob-

299   served peak values range from 100 $\mu A/m^2$ (Rother's threshold value) to 2000 $\mu A/m^2$.

300   E_0 was scaled up to 1500 mV/m to bracket a likely upper limit on thermospheric

301   upwelling in the simulations with Alfvénic heating described in Sec. 3. Note that the ac-

302   tual electric field amplitude calculated from (9) is much less than E_0 owing to the mode

303   number dependence in the denominator of (11).

304 Model time series and spectra obtained from the above procedure, using profiles for the back-

305 ground parameters specified in the next section, are described in the Supporting Information,

306 Text S5 and Figs. S3 and S4.

2.3 Specification of background parameters

308   FDTD solutions to (7) and (8) require specification of the altitude profiles (z dependence)

309 for parameters σ_P, σ_0 and ε. We determined these parameters from equations (4)-(6) using the

310 most recent International Reference Ionosphere (IRI-2016) (Bilitza 2018), the Navy Research

311 Lab Mass Spectrometer and Incoherent Scatter radar (NRLMSISE-00, or MSIS) model (Picone

312 et al., 2002) and an Earth-centered dipole model for the geomagnetic field. The IRI model uses

313 the date to look up historical data of daily F10.7, a measure of solar activity by measuring the

314 solar radio flux at 10.7 cm as a proxy of solar activity. The MSIS model similarly uses F10.7, as

315 well as user-input for the 3-hour Ap, a proxy of the planetary magnetic field for which historical

316 data exists.

317   Two different profiles for σ_P, σ_0 and ε were computed at the average cusp location (giv-

318 en by its MLT-MLAT center) at 12:00 UT on 26 March 2003 and on 27 March 2003 in a base-

319 line CMIT run without Alfvénic heating. The first day exhibits weak-to-moderate solar

320 wind/IMF driving. More intense SIR activity in the interplanetary medium is very prominent

321 during the second day (Fig. 2). The electron density computed by IRI is scaled such that the peak

322 electron density (NmF2) matches the peak in the average electron density profile in CMIT in the

323 cusp region for the same 24-hour period. This rescaling of the plasma density from IRI values to

324 the mean CMIT values for each day of the simulated interval is a step toward self-consistency of

325 the parameterized model and CMIT.

326   MSIS determines the thermosphere only up to 1000 km altitude. Above this altitude colli-

327 sional effects are negligible and the collisionless Alfvén speed $\left(B/\sqrt{\mu_0 \sum_s m_s n_s}\right)$ is used up to

328 2000 km. Above 2000 km altitude, the Alfvén speed is set to a constant, equal to its value at

329 2000 km. The Pedersen conductivity is interpolated on a log-linear scale between 1000 and 2000

330 km altitude using the conductivity calculated using MSIS-IRI at 1000 km and a specified small

331 value ($1.88\text{x}10^{-12}$ S/m) at 2000 km altitude – the value in Lotko & Zhang (2018). The results are

332 insensitive to this value as long as it is small. Above 2000 km we set σ_P uniform to its value at

333 2000 km. The parallel conductivity is interpolated on a log-linear scale from its computed value

334 at 1000 km to a large value at the top of the simulation space such that η becomes negligible; σ_0

335 $= 1\text{x}10^{10}$ S/m was chosen. At altitudes below 90 km, below the range of CMIT, the Alfvén speed

336 is set to a constant equal to 12000 km/s. The wave speed is actually larger than 12000 km/s in the

337 lower thermosphere, approaches the speed of light in the lower atmosphere and is artificially lim-

338 ited here for numerical efficiency. This choice does not influence the results in the IT region of

339 interest. The conductivity profiles are interpolated on a log-linear scale between computed values

340 at 90 km and 0 km altitude where both Pedersen and parallel conductivities are set to $6\text{x}10^{-12}$ S/m

341 (Lysak 1999, Lotko & Zhang, 2018). The wave solution at *E-* and *F*-region altitudes is relatively

342 insensitive to the value specified for conductivities at Earth's surface, provided it is small com-

343 pared to their values above 90 km.

344   The altitude profiles of σ_P, σ_0 and wave speed V_A used to compute FDTD solutions for

345 the Alfvén wave fields are included in Figure S5 of the Supporting Information.

346 **2.4 Integrating Alfvén wave heating into CMIT**

347   The Alfvén wave solution, observationally constrained as described in the previous sec-

348 tion, is used to augment CMIT's Joule heating rate as a function of altitude. To this end, we use

349 the fact that time scale for ion acceleration by the Alfvénic fluctuations (wave periods ≤ 20 sec)

350 is short compared to the time scale for neutral-fluid acceleration ($\nu_{ni}^{-1} > 1$ hour). This disparity in

351 time scale renders the Alfvén wave-induced quiver velocity of the neutral gas—mediated by ion-

352 neutral friction—negligible compared to the perturbed ion velocity for the considered range of

353 wave frequencies (0.5-2 Hz) and IT conditions described in Sec. 2.3 (see SI Text S3 and Fig.

354 S2). In this case, the effects of Alfvén wave acceleration on ion-neutral friction may be neglected

355 in the neutral gas momentum equation, and the neutral gas may be considered stationary when

356 evaluating the Alfvénic contribution to Joule heating (SI Text S3). Also making use of the ine-

357 qualities $\omega^2, \omega \nu_i \ll \Omega_i^2$ that underlie the derivation of (1)-(3), the Alfvénic Joule heating rate

358 $Q_{J,A}$ may be calculated as $\sigma_P \delta E_A^2$ (see SI Text S7).

359   Rather than specifying a particular realization of the Alfvénic fluctuations encountered

360 by the neutral fluid as it traverses the cusp region, we characterize the fluctuations in terms of an

361 ensemble average over all possible random phases in (9) to obtain the Alfvénic Joule heating rate

362 in terms of the RMS amplitude of the fluctuations:

$$
\begin{aligned}
Q_{J,A}(z) &= \sigma_P \left\langle E_x^2(x,z,t) \right\rangle_{x,t} \\
&= \sigma_P \frac{1}{\lambda_{\max}} \int_0^{\lambda_{\max}} dx \frac{1}{\tau_{\max}} \int_0^{\tau_{\max}} dt\, E_x^2(x,z,t) \\
&= \frac{\sigma_P}{4} \sum_{m,n} E_{m,n}^2(z) \equiv \sigma_P \delta E_{A,rms}^2 .
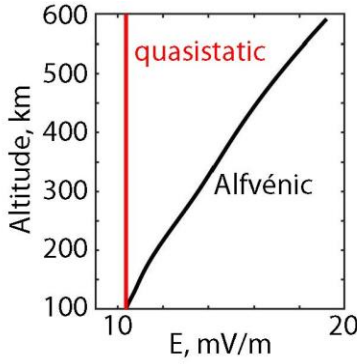\end{aligned}
\tag{12}
$$

363

Figure 3. Altitude profile of the rms Alfvén wave electric field $\delta E_{A,rms}$ for day 2 of the event compared to that of a (quasi)static electric field with the same amplitude in the *E* region.

364   The average profile for the root-mean-square (RMS) Alfvénic electric field, $\delta E_{A,rms}$, is precom-

365   puted twice by the FDTD Alfvén wave solver, at 12:00 UT on 26 March 2003 and on 27 March

366   2003, at the average cusp locations where the σ_P profiles were determined from the TIEGCM-

367   scaled, MSIS-IRI data as described in Sec. 2.3. These two representative $\delta E_{A,rms}$ profiles are

368   taken to be constant in *x* and *t* throughout the corresponding day and over the instantaneous cusp

369   area determined by LFM's cusp finding algorithm (Zhang et al., 2013). While the Alfvén wave

370   power flowing into CMIT's cusp area is actually bursty in space and time, the thermosphere ef-

371   fectively integrates over the Alfvénic heating during its relatively slow transit through the cusp.

372   Thus a space-time average for parameterized Alfvénic heating of the thermosphere is appropri-

373   ate. The profile obtained for $\delta E_{A,rms}$ for day 2 of the event is shown in Figure 3 along with that

374   of a static electric field with the same value in the *E* region for comparison. The Alfvénic electric

375   field is $\approx 50\%$ larger at *F*-region altitudes than a static electric field of comparable intensity in

376   the *E*-region ionosphere owing to the effect of the IAR. IAR modes at frequencies greater than $\approx$

377   0.5 Hz are efficiently pumped by the driver, and they intensify upon being trapped by the strong

378   opposing gradients in wave speed in the *F* region (cf. Figs. 2 and 3 of Lotko & Zhang, 2018).

379   The RMS electric field $\delta E_{A,rms}$ from the Alfvén wave model is integrated into the Joule

380   heating module of CMIT by augmenting the Joule heating per unit mass for the neutral $\left(Q_J^{T_N} \right)$

381   and ion $\left(Q_J^{T_i}\right)$ gasses according to the formulae

$$Q_J^{T_N} = \frac{\sigma_P B^2}{\rho}\left[C_J\left(\mathbf{v}_{E\times B} - \mathbf{v}_{n\perp}\right)^2 + \frac{\delta E_{A,rms}^2}{B^2}\right], \tag{13}$$

$$Q_J^{T_i} = \frac{\bar{m}_n}{\bar{m}_n + \bar{m}_i}Q_J^{T_n} . \tag{14}$$

384   The Pedersen conductivity σ_P in $Q_J^{T_N}$ is calculated by CMIT at each TIEGCM time step (5 sec-

385   onds), ρ is the thermospheric mass density from TIEGCM, B is the geomagnetic field (the Inter-

386   national Reference Geomagnetic Field is used in TIEGCM), $\mathbf{v}_{ExB}$ and $\mathbf{v}_{n_\perp}$ are, respectively, the

387   ion $E\times B$ drift velocity and the neutral wind velocity perpendicular to B, both derived from

388   CMIT, and $\bar{m}_n$ and $\bar{m}_i$ are the mean molecular mass of neutrals and ions, respectively. Equation

389   (13) is the Joule heating rate in the reference frame of the neutral gas, which is equivalent to the

390   frictional heating rate due to ion-neutral drag (see SI Text S7). For the reasons discussed in SI

391   Text S3, the neutral gas may be considered stationary when evaluating the Alfvénic contribution

392   to Joule heating, i.e., the second term on the right side of (13).

393   The basic Joule heating module in TIEGCM includes the constant multiplicative factor

394   (C_J) that augments the Joule heating specified by the first term in (13). This factor is intended to

395   model the effects of quasistatic subgrid variability in the Joule heating (e.g., Figure 1) and effec-

396   tively adds subgrid Joule heat where TIEGCM produces grid-resolved Joule heat. Although this

397   simple scaling for the subgrid Joule heat is not likely to be accurate in detail, it improves

398   TIEGCM's baseline prediction for the thermospheric mass density. The addition of the parame-

399   terized Alfvénic heating model in CMIT also captures subgrid heating processes, so we reduced

400   the nominal value $C_J = 1.5$ in the default TIEGCM code to 1.35. A time-dependent, assimilative

401   adjustment of C_J, as in the assimilation method of Sutton (2018), may further improve the fideli-

402   ty of the baseline prediction.

403   Even though $\delta E_{A,rms}$ is constant during each day of the SIR event, the Alfvénic Joule

404   heating rate evolves in CMIT as TIEGCM evolves because $Q_{J,A}(z)$ in (13) is calculated using

405   TIEGCM's σ_P. This Alfvén wave coupling dynamically modulates Joule heating because the

406   CMIT-determined σ_P changes with dynamic variations in electron precipitation and ion-neutral

407   chemistry, both of which are at play during the simulated SIR event. In theory and possibly in

408   the future, both $\delta E_{A,rms}$ and $Q_{J,A}(z)$ could be regulated at the cadence of a CMIT time step by

409   regulating the Alfvén wave driver amplitude in the FDTD solver using LFM's Alfvén wave

410   Poynting flux module (Zhang et al., 2015b) and TIEGCM's IT dynamic state. The approach im-

411   plemented here may be considered a proof-of-concept to determine the value of continuing such

412   future developments.

413

414   **3. Results and Discussion**

415   We first ran CMIT for 48 hours for the solar and interplanetary conditions during 26-27

416   March 2003 without the Alfvénic heating term in equation (13). This run provides a baseline for

417   comparing changes when Alfvénic heating is included in CMIT.
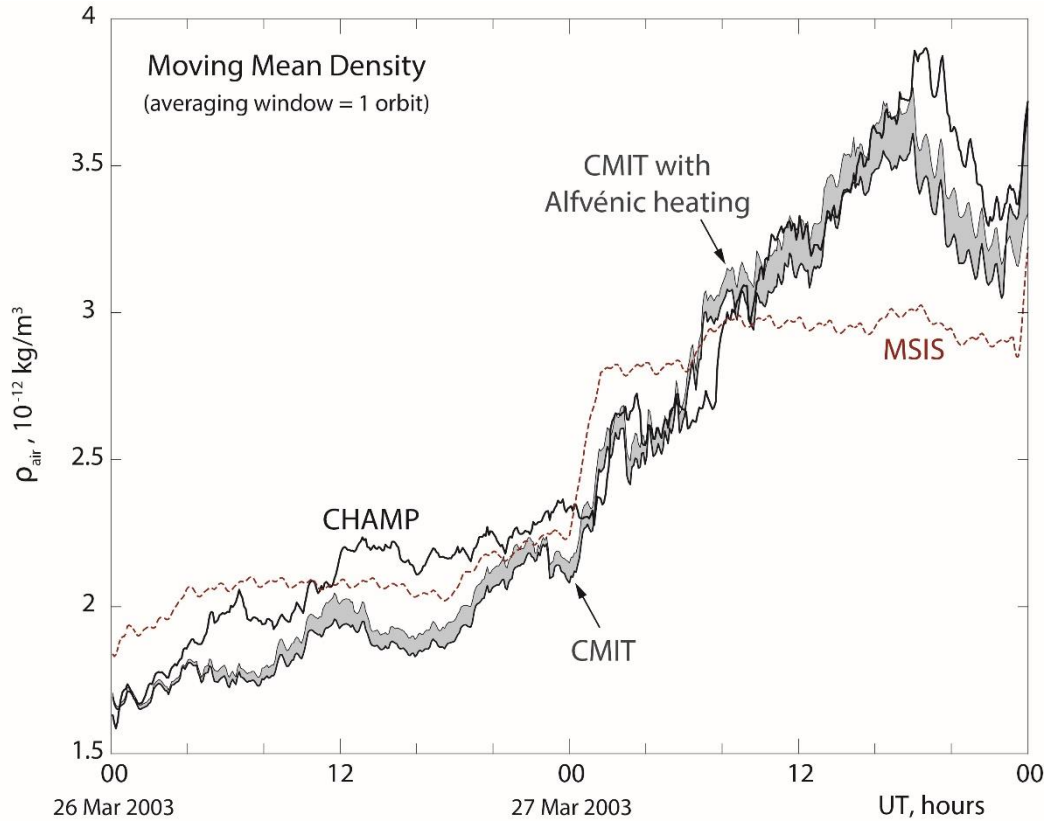
Figure 4. One-orbit moving mean of CHAMP-derived thermospheric mass density for 26-27 March 2003, CMIT simulated thermospheric density along the CHAMP orbit, with and without Alfvénic heating, and the MSIS prediction of the density along the CHAMP orbit. The curve labeled CMIT is the baseline run. CMIT with Alfvénic heating is the run with average peak FAC of 1 mA/m^2. Gray area between them indicates the expected range for CMIT density enhancement with Alfvénic heating effects.

418   A one-orbit moving mean of the CHAMP data and CMIT results (Figure 4) was evaluat-

419   ed to gain an overview of cumulative effects and hour-scale trends in the thermospheric response

420   to the SIR event. The IMF activity and solar wind driving are weak to moderate during the first

421   24 hours (26 March 2003) of the event, and the air density recorded along the CHAMP orbit in-

422   creases modestly during the day, from about 1.6×10^{-12} kg/m^3 to 2.3×10^{-12} kg/m^3. CMIT under-

423 predicts the density by as much as 15% during the first day. Two curves are plotted for CMIT in

424 Fig. 4 to bracket its prediction. The curve labeled CMIT is the baseline estimate. The curve la-

425 beled CMIT with Alfvénic heating is calculated for an RMS wave electric field ($\delta E_{A,rms}$) that

426 yields a peak Alfvénic FAC of 1 mA/m^2 ($E_0 = 1500$ mV/m in equation 11). The CMIT estimate

427 for the orbit-average mass density of the neutral gas lies in the gray area between the two curves.

428 The MSIS prediction is also plotted in Fig. 4 for comparison.

429   Around 18:00 UT on 26 March, both the IMF activity and solar wind driving pick-up (cf.

430 Fig. 2). The latency in the response of the thermosphere along this particular orbit is about 6

431 hours, after which the thermospheric density observed by CHAMP, simulated by CMIT and es-

432 timated by MSIS all begin a comparatively steep increase shortly after 00:00 UT on March 27

433 (cf. Fig. 4). All three estimates of the air density exhibit a relative maximum just after 18:00 UT

434 on 27 March. CHAMP registers a density of 3.9×10^{-12} kg/m^3 at this time; the corresponding

435 MSIS estimate is near 3.0×10^{-12} kg/m^3 while the CMIT prediction ranges from 3.6 to 3.8×10^{-12}

436 kg/m^3. CMIT clearly tracks the CHAMP density more closely during the second day of the

437 event. As expected the CMIT prediction is more dynamic than MSIS – a consequence of the mi-

438 nute-cadence interplanetary dynamics driving CMIT vs. the daily F10.7 and 3-hour Ap indices

439 parameterizing MSIS.

440   The increase in air density due to Alfvénic heating relative to baseline is larger during the

441 second day of the event than during the first day, with a maximum difference of 0.08×10^{-12}

442 kg/m^3 during the first day and 0.15×10^{-12} kg/m^3 during the second day. However, the maximum

443 difference over baseline is ≈ 4% on both days because the baseline is greater on the second day.

444 The larger increase in density from Alfvénic heating on the second day is due in part to an in-
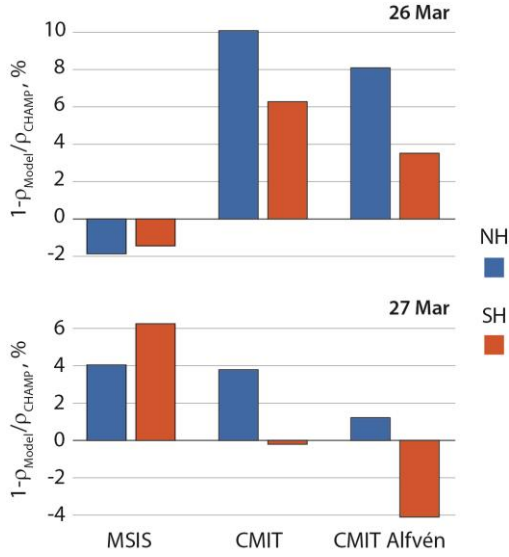
445 crease in TIEGCM's Pedersen conductivity.

Figure 5. Comparison of daily mean error (in %) in model predictions relative to CHAMP's air density for MSIS, CMIT (baseline) and CMIT with Alfvénic heating for each hemisphere (NH, SH) and event day (26, 27 March).

446   To quantify the average daily cumulative error in model predictions, we calculated the in-

447   stantaneous error $(1 - \rho_{\text{Model}}/\rho_{\text{CHAMP}})$ along the CHAMP orbit and then determined the daily

448   average error for each hemisphere (Figure 5). By this measure, MSIS performs better than CMIT

449   for weak-to-moderate activity (26 March), with Alfvénic heating decreasing CMIT's relative er-

450   ror by $\approx 2\%$ in both hemispheres. For higher activity (27 March), CMIT performs better than

451   MSIS. Including Alfvénic heating in CMIT decreases its error by $\approx 3\%$ in the NH on 27 March,

452   but it increases the error by 4% in the SH. We attribute the reduction in error when Alfvénic

453   heating is included, in part, to the increased Joule heating resulting from the increase in CMIT's

454   Pedersen conductivity. The increase in error in the SH during 27 March may be due in part to

455   inconsistencies in CMIT's treatment of the geomagnetic field, which is based on the Internation-

456   al Geomagnetic Reference Field in TIEGCM and on a Earth-centered dipole field in the LFM

457   and MIX solvers. TIEGCM includes the intrinsic NH/SH asymmetries of the IGRF, but LFM

458   and MIX drive TIEGCM with inputs from the magnetosphere that ignore this asymmetry.

459   We also compared the instantaneous air density recorded on CHAMP with CMIT and

460   MSIS predictions. The left panel of Figure 6 shows CMIT diagnostics for the air density on 27

461   March 2003 in the northern hemisphere (NH) at the CHAMP altitude (413 km). At 0815 UT

462   CHAMP traverses the edge of a dayside density enhancement in the CMIT thermosphere includ-

463   ing the effects of cusp-region Alfvénic heating (Fig. 6A). The point of closest approach at 0815

464   UT is indicated by the black circle located at 18.7 MLT and 81.0° MLAT. Fig. 6B compares the

465   instantaneous air densities from CHAMP measurements, CMIT predictions and MSIS estimates

466   along the CHAMP orbit vs UT. As in Fig. 4, the curve labeled CMIT is for the baseline run,

467   while the curve labeled CMIT with Alfvénic heating is the CMIT run with a peak Alfvénic FAC

468   of 1 mA/m^2. The gray area between these two curves indicates the expectd range of CMIT pre-

469   dictions with Alfvénic heating. Fig. 6C is a NH map of the % difference in CMIT's predictions

470   with and without Alfvénic heating: $\Delta(\text{CMIT}) = \rho_{Alfvén}/\rho_{baseline} - 1$. The maximum density

471   difference in Fig. 6B is about 12%, but the main cusp density enhancement (not traversed by

472   CHAMP) exhibits a difference closer to 20% in Fig. 6C. Changes in thermospheric density re-

473   sulting from Alfvénic heating are not localized to the cusp or the dayside. The largest difference

474   occurs between about 0200 and 0600 MLT near 80° MLAT. The effects of co-rotation and neu-

475   tral winds evidently redistribute the additional cusp density enhancement produced by Alfvénic

476   heating.

477   The right panels of Fig. 6 continue the analysis in the same format for the subsequent

478   CHAMP crossing of the NH. CHAMP traverses the edge of the density enhancement in CMIT at

479   9.67 MLT and -69.5° MLAT at 0955 UT (black circle in Fig. 6D). The comparison between

480   CHAMP measurements, CMIT prediction and MSIS estimate along the orbit (Fig. 6E) shows

481   that CMIT predicts the location of CHAMP's peak density in both hemispheres, and its accuracy

482   improves with Alfvénic heating included. This feature is missed entirely by MSIS, which exhib-

483   its a relative minimum where both the CHAMP and MSIS densities peak. The maximum density

484   difference for CMIT with and without Alfvénic heating is about 14% in Fig. 6E. As for the pre-

485   vious NH crossing, the main cusp density enhancement (which CHAMP does not traverse) ex-

486   hibits a larger difference closer to 30% in Fig. 6F, and the redistribution and modification of the

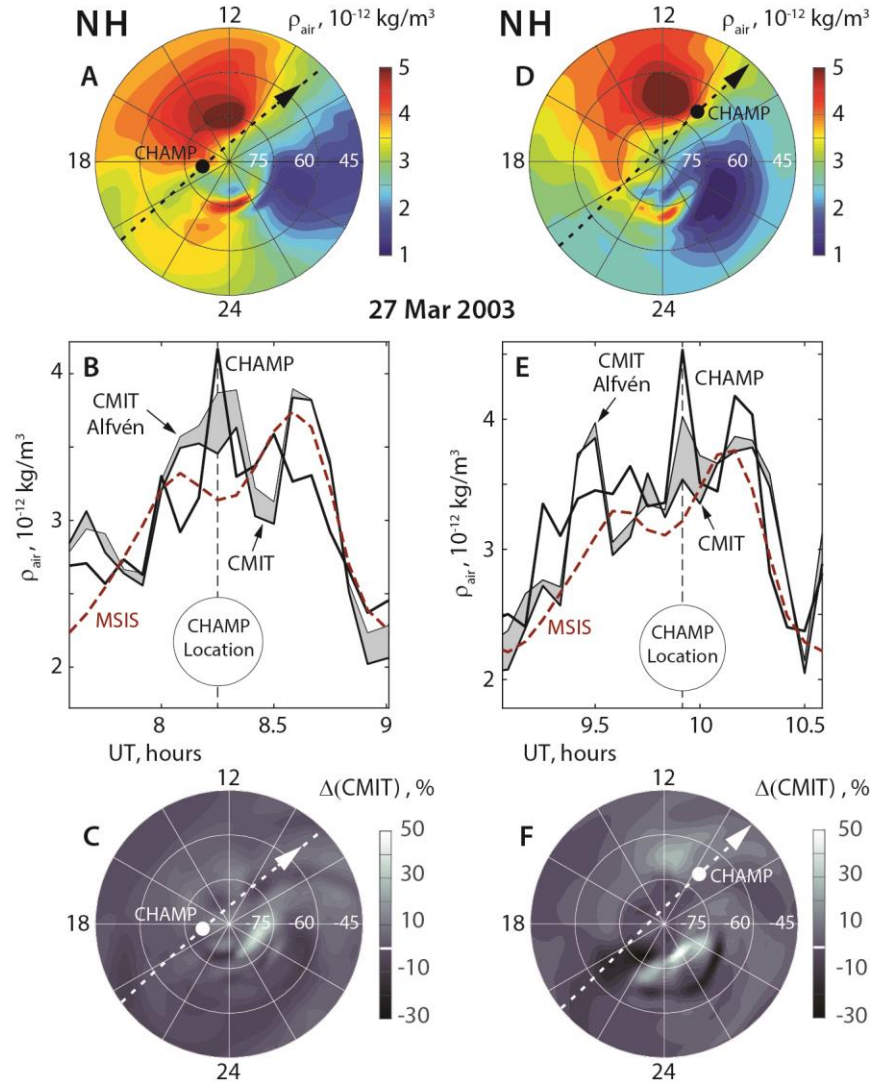487   Alfvénic-enhanced density is prominent throughout the nightside polar region.

Figure 6. Air density along consecutive CHAMP orbits in the northern hemisphere (NH) on 27 March 2003 when CHAMP passes through the edges of high-latitude density enhancements. **A:** Simulated air density (color) at the CHAMP altitude ($\approx$ 413 km) vs MLT and MLAT at the UT corresponding to "CHAMP Location" in panel B. Black circle indicates location of CHAMP at that UT. **B:** Comparison of instantaneously observed, simulated and MSIS air density vs. UT. CMIT curve is the baseline run. Curve labeled "CMIT Alfvén" is a run with a peak Alfvénic FAC of 1 mA/m^2. As in Fig. 4 gray area indicates expected range of CMIT predictions with Alfvénic heating. **C:** % difference in CMIT air density with and without Alfvénic heating. $\Delta(\text{CMIT}) = \rho_{Alfvén}/\rho_{baseline} - 1$. Panels **D**, **E** and **F** in same format.

4. Conclusions

489

490   • CMIT tracks orbit-averaged air density at CHAMP altitudes more closely than MSIS

491   during intervals of solar wind and IMF activity characteristic of an SIR event (Fig. 4).

492 When comparing the IT response during the less active, first day of the simulated SIR event to

493 the response during the more active second day, we find that CMIT replicates CHAMP-derived

494 density measurements better than MSIS during the more active period. This finding is not sur-

495 prising because the proxy-governed nature of MSIS relies on inputs of average parameters over

496 longer periods (multi-hour to days) and is not as responsive to interplanetary variability as CMIT

497 when driven by one-minute solar wind and IMF data. The MIT coupling intrinsic to CMIT al-

498 lows effects such as soft electron precipitation, electric field variability and Alfvénic heating to

499 modify the Pedersen conductivity, Joule heating rate and, therefore, air temperature and density

500 in the cusp region on faster time scales than MSIS.

501   • Alfvénic heating modestly improves CMIT's daily mean prediction of orbit-averaged

502   air density relative to CHAMP measurements (Fig. 5) and produces 20-30% regional

503   enhancements in the high-latitude thermospheric density relative to a CMIT simula-

504   tion without Alfvénic heating (Fig. 6 bottom panels).

505 Inclusion of Alfvénic heating effects in CMIT decreases its daily mean error by 2-3% in orbit-

506 averaged air density relative to measurements along a particular CHAMP orbit, except in the

507 southern hemisphere during the active second day of the SIR event when the error increased by

508 4%. This discrepancy may arise in part from the nonconforming geomagnetic field models used

509 in CMIT's three component models, which treat geomagnetic hemispheric asymmetry different-

510 ly. Enhancements of 20-30% in air density are seen throughout the high-altitude region (not just

511 the cusp region) relative to a baseline CMIT run. This finding suggests that, during the course of

512 the two-day long simulation, co-rotation and neutral winds redistribute the additional cusp densi-

513   ty enhancements produced by Alfvénic heating.

514   • Alfvénic heating produces significant thermospheric density enhancements at

515   CHAMP altitudes in and near the cusp during times of intense Alfvénic Poynting flux

516   (Fig. 6 middle panels).

517   Alfvénic thermospheric heating is especially effective when magnetopause variability induced by

518   solar wind and IMF activity stimulates intense Alfvénic Poynting fluxes flowing into the low-

519   altitude cusp. The resulting Alfvén wave energy deposition in the ionospheric Alfvén resonator

520   adds to the important effects of soft electron precipitation and quasistatic electric field variability

521   on *F*-region Joule heating and thermospheric upwelling previously reported in the literature.

522   These relatively fast dynamic effects operating in concert may explain the anomalous thermo-

523   spheric densities CHAMP recorded relative to the MSIS empirical model (Liu et al., 2005). A

524   detailed analysis showed that MSIS completely misses the air density enhancements registered

525   by both CHAMP and CMIT along near cusp orbits; and CMIT with Alfvénic heating substantial-

526   ly improves CMIT's baseline prediction of the enhancements (by 10-15%). During this SIR

527   event, CHAMP did not actually traverse the central cusp region where CMIT's density en-

528   hancements with Alfvénic heating are even larger (20-30%) than without it.

529

536   plots shown including CHAMP, MSIS, and CMIT data is available publicly:

543

References

545   Bilitza, D. (2018), IRI the International Standard for the Ionosphere. *Advanced Radio Science*,

546   *16*, 1-11. https://doi.org/10.5194/ars-16-1-2018.

547   Brinkman, D. G., R. L. Walterscheid, J. H. Clemmons, & J. H. Hecht (2016), High-resolution

548   modeling of the cusp density anomaly: Response to particle and Joule heating under typical

549   conditions. *Journal of Geophysical Research: Space Physics*, *121*, 2645-2661.

550   https://doi.org/10.1002/2015JA021658.

551   Chaston, C. C., Bonnell, J. W., Carlson, C. W., McFadden, J. P., Ergun, R.E., & Strangeway,

552   R. J. (2003). Properties of small-scale Alfvén waves and accelerated electrons from FAST.

553   *Journal of Geophysical Research, 108*(A4), 8003 https://doi.org/10.1029/2002JA009420.

554   Chaston, C. C., Carlson, C. W., McFadden, J. P., Ergun, R. E., & Strangeway, R. J. (2007).

555   How important are dispersive Alfvén waves for auroral particle acceleration? *Geophysical*

556   *Research Letters, 34*, L07101. https://doi.org/10.1029/2006GL029144.

557   Clemmons, J. H., Hecht, J. H., Salem, D. R., & Strickland D. J. (2008). Thermospheric Densi-

558   ty in the Earth's Magnetic Cusp as Observed by the Streak Mission. *Geophysical Research*

559   *Letters*, *35*, L24103. https://doi.org/10.1029/2008gl035972.

560   Dang, T., Lei, J., Wang, W., Burns, A., Zhang, B., & Zhang, S.-R. (2018). Suppression of the

561   polar tongue of ionization during the 21 August 2017 solar eclipse. Geophysical Research

562   Letters, 45, 2918–2925. https://doi.org/ 10.1002/2018GL077328.

563   Deng, Y., Fuller-Rowell, T. J., Ridley, A. J., Knipp, D., & Lopez, R. E. (2013). Theoretical

564   study: Influence of different energy sources on the cusp neutral density enhance-

565   ment. *Journal of Geophysical Research: Space Physics*, *118*, 2340-2349.

566   https://doi.org/10.1002/jgra.50197.

567   Hatch, S. M., LaBelle, J., Lotko, W., Chaston, C. C., & Zhang, B. (2017). IMF control of Alf-

568   vénic energy transport and deposition at high latitudes. *Journal of Geophysical Research:*

569   *Space Physics, 122*, 12,189–12,211. https://doi.org/10.1002/2017JA024175.

570   Ishii, M., Sugiura, M., Iyemori, T., & Slavin, J. A. (1992). Correlation between magnetic and

571   electric field perturbations in the field-aligned current regions deduced from DE 2 observa-

572   tions. *Journal of Geophysical Research, 97*(A9), 13,877–13,887. https://doi.org/10.1029/

573   92JA00110.

574   Jee, G., Burns, A. G., Wang, W., Solomon, S. C., Schunk, R. W., Scherliess, et

575   al. (2008). Driving the TING model with GAIM electron densities: Ionospheric effects on

576   the thermosphere. *J. Geophys. Res.*, *113*, A03305, https://doi.org/10.1029/2007JA012580.

577   Jian, L., Russel, C. T., Luhmann, J. G., & Skoug, R. M. (2006). Properties of stream interac-

578   tions at one AU during 1995–2004. *Solar Physics*, 239(1-2), 337–392.

579   https://doi.org/10.1007/s11207-006-0132-3.

580   Keiling, A., Wygant, J. R., Cattell, C. A., Mozer, F. S., & Russell, C. T. (2003). The global

581   morphology of wave Poynting flux: Powering the aurora. Science, 299(5605), 383–386.

582   https://doi.org/10.1126/science.1080073.

583   Kervalishvili, G. N., & Lühr, H. (2013). The relationship of thermospheric density anomaly

584   with electron temperature, small-scale FAC, and ion up-flow in the cusp region, observed

585   by CHAMP and DMSP satellites. *Annales de Geophysique, 31*(3), 541–554.

586   https://doi.org/10.5194/angeo-31-541-2013.

587 Kervalishvili, G. N. & Lühr, H. (2014). Climatology of zonal wind and large-scale FAC with

588   respect to the density anomaly in the cusp region: seasonal, solar cycle, and

589   IMF B_y dependence. *Ann. Geophys., 32*, 249–261, https://doi.org/10.5194/angeo-32-249-

590   2014.

591 Liu, H., Lühr, H., Henize, V., & Köhler, W. (2005). Global distribution of the thermospheric

592   total mass density derived from CHAMP. *Journal of Geophysical Research, 110,* A04301.

593   https://doi.org/10.1029/2004JA010741.

594 Liu, J., Wang, W., Zhang, B., Huang, C., & Lin, D. (2018). Temporal variation of solar wind

595   in controlling solar wind-magnetosphere-ionosphere energy budget. *Journal of Geophysi-*

596   *cal Research: Space Physics*, 123, 5862– 5869. https://doi-

597   org.cuucar.idm.oclc.org/10.1029/2017JA025154.

598 Lotko, W., & Zhang, B. (2018). Alfvénic heating in the cusp ionosphere-thermosphere. *Jour-*

599   *nal of Geophysical Research: Space Physics*, 123. https://doi.org/10.1029/2018JA025990

600 Lyon, J.G., Fedder, J. A., & Mobarry, C. M., (2004). The Lyon–Fedder–Mobarry (LFM)

601   Global MHD Magnetospheric Simulation Code. *Journal of Atmospheric and Solar-*

602   *Terrestrial Physics*, *66*(15-16), 1333–1350. https://doi.org/10.1016/j.jastp.2004.03.020.

603 Lysak, R. L. (1991). Feedback instability of the ionospheric resonant cavity. *Journal of Geo-*

604   *physical Research, 96*(A2), 1553–1568. https://doi. org/10.1029/90JA02154.

605 Lysak, R. L. (1999). Propagation of Alfvén waves through the ionosphere: Dependence on

606   ionospheric parameters. *Journal of Geophysical Research, 104(*A5), 10,017–10,030.

607   https://doi.org/10.1029/1999JA900024.

608   Lühr, H., Warnecke, J. F. & M. K. A. Rother, M. K. A. (1996). An algorithm for estimating

609   field-aligned currents from single spacecraft magnetic field measurements: a diagnostic

610   tool applied to Freja satellite data. *IEEE Transactions on Geoscience and Remote Sensing,*

611   *34(*6), 1369-1376, https://doi.org/10.1109/36.544560.

612   Lühr, H., Rother, M., Köhler, W., Ritter, P., & Grunwaldt, L. (2004). Thermospheric

613   upwelling in the cusp region: Evidence from CHAMP observations. *Geophysical Research*

614   *Letters, 31,* L06805. https://doi.org/10.1029/2003GL019314.

615   Lühr, H., Park, J., Gjerloev, J. W., Rauberg, J., Michaelis, I., G. Merayo, J. M.,& Brauer,

616   P. (2015). Field-aligned currents' scale analysis performed with the Swarm constella-

617   tion. *Geophys. Res. Lett., 42*, 1– 8, https://doi.org/10.1002/2014GL062453.

618   Park, J., Lühr, H., Knudsen, D. J., Burchill, J. K., & Kwak, Y.-S. (2017). Alfvén waves in the

619   auroral region, their Poynting flux, and reflection coefficient as estimated from Swarm ob-

620   servations. *Journal of Geophysical Research: Space Physics*, *122*, 2345– 2360,

621   https://doi.org/10.1002/2016JA023527.

622   Matsuo, T., & Richmond, A. D. (2008). Effects of high-latitude ionospheric electric field vari-

623   ability on global thermospheric Joule heating and mechanical energy transfer rate. *Journal*

624   *of Geophysical Research, 113,* A07309. https://doi.org/10.1029/2007JA012993.

625   Merkin, V. G., & Lyon, J. G., (2010). Effects of the Low-Latitude Ionospheric Boundary

626   Condition on the Global Magnetosphere. *Journal of Geophysical Research: Space Physics*,

627   *115*(A10). https://doi.org10.1029/2010ja015461.

628   Mur, G. (1981). Absorbing boundary conditions for the finite-difference approximation of the

629   time-domain electromagnetic-field equations. *IEEE Transactions on Electromagnetic*

630   *Compatibility*, *EMC-23*(4), 377–382. https://doi.org/10.1109/TEMC.1981.303970.

631   Picone, J. M., A. E. Hedin, D. P. Drob, & A. C. Aikin, (2002). NRLMSISE-00 empirical

632   model of the atmosphere: Statistical comparisons and scientific issues. *Journal of Geo-*

633   *physical Research: Space Physics*, *107*(A12), 1468, https://doi.org/10.1029/2002JA009430

634   Qian, L., et al. (2013). The NCAR TIE-GCM: A Community Model of the Coupled Thermo-

635   sphere/Ionosphere System, in *Modeling the Ionosphere-Thermosphere System,* ed. by J.D

636   Huba, R.W. Schunk & G.V. Khazanov, Geophysical Monograph Series 201, AGU, Wash-

637   ington D.C. https://doi.org/10.1029/2013GM001452.

638   Rentz S., & Lühr H. (2008). Climatology of the cusp-related thermospheric mass density

639   anomaly, as derived from CHAMP observations. *Annales Geophysicae. 26*(9), 2807-2823.

640   https://doi.org/10.5194/angeo-26-2807.

641   Rother, M., Schlegel, K., & Lühr, H. (2007). CHAMP observation of intense kilometer-scale

642   field-aligned currents, evidence for an ionospheric Alfvén resonator. *Annales de Geophy-*

643   *sique, 25*(7), 1603–1615. https://doi.org/10.5194/angeo-25-1603-2007.

644   Schunk, R., & Nagy, A. (2009). *Ionospheres, 2nd Edition*, Ch. 4. Cambridge, UK: Cambridge

645   University Press.

646   Stawarz, J. E., Eriksson, S., Wilder, F. D., Ergun, R. E., Schwartz, S. J., Pouquet, A., Burch, J.

647   L., et al. (2016). Observations of turbulence in a Kelvin Helmholtz event on 8 September

648   2015 by the Magnetospheric Multiscale mission. *Journal of Geophysical Research: Space*

649   *Physics, 121*, 11,021–11,034. https://doi.org/10.1002/2016JA023458.

650   Sutton, Eric K (2018). A New Method of Physics-Based Data Assimilation for the Quiet and

651   Disturbed Thermosphere. *Space Weather*, *16*(6), 736–753.

652   https://doi.org/10.1002/2017sw001785.

653   Trakhtengerts, V. Y. & Fel'Dshtein, A. Y. (1987). Turbulent regime of magnetospheric con-

654   vection. *Geomagnetism and Aeronomy*, *27*(2), 221-225.

655   Tu, J., Song, P., & Vasyliūnas, V. (2011). Ionosphere/thermosphere heating determined from

656   dynamic magnetosphere-ionosphere/thermosphere coupling. *Journal of Geophysical Re-*

657   *search, 116*, A09311. https://doi.org/10.1029/2011JA016620.

658 Wang, W., Wiltberger, M., Burns, A. G., Solomon, S. C., Killeen, T. L., Maruyama, N., &

659   Lyon, J. G. (2004). Initial results from the Coupled Magnetosphere–Ionosphere–

660   Thermosphere Model: Thermosphere–ionosphere responses. *Journal of Atmospheric and*

661   *Solar-Terrestrial Physics*, *66*(15-16), 1425–1441.

662   https://doi.org/10.1016/j.jastp.2004.04.008.

663 Wang, W., Lei, J., Burns, A. G., Wiltberger, M., Richmond, A. D., Solomon, S. C., Killeen, T.

664   L., Talaat, E. R., & Anderson, D. N. (2008). Ionospheric electric field variations during a

665   geomagnetic storm simulated by a coupled magnetosphere ionosphere thermosphere

666   (CMIT) model. *Geophysical Research Letters*, *35*, L18105.

667   https://doi.org/10.1029/2008GL035155.

668 Wiltberger, M., Pulkkinen, T. I., Lyon, J. G., & Goodrich, C. C. (2000). MHD simulation of

669   the magnetotail during the December 10, 1996, substorm. *Journal of Geophysical Re-*

670   *search*, *105*(A12), 27649– 27663, https://doi.org/10.1029/1999JA000251.

671 Wiltberger, M., Wang, W., Burns, A.G., Solomon, S.C., Lyon, J. G., & Goodrich, C. C.

672   (2004). Initial results from the coupled magnetosphere-ionosphere-thermosphere model:

673   Magnetospheric and ionospheric responses. *Journal of Atmospheric and Solar-Terrestrial*

674   *Physics*, *66*(15-16), 1411-1423, https://doi.org/10.1016/j.jastp.2004.03.026.

675 Zhang, B., Lotko, W., Brambles, O., Wiltberger, M., Wang, W., Schmitt, P., & Lyon, J.

676   (2012). Enhancement of thermospheric mass density by soft electron precipitation. *Geo-*

677   *physical Research Letters, 39,* L20102. https://doi.org/10.1029/2012GL053519.

678 Zhang, B., Brambles, O., Lotko, W., Dunlap-Shohl, W., Smith, R., Wiltberger, M., & Lyon,

679   J. (2013). Predicting the location of polar cusp in the Lyon-Fedder-Mobarry global magne-

680   tosphere simulation. *Journal of Geophysical Research: Space Physics*, *118*, 6327–6337.

681   https://doi.org/10.1002/jgra.50565.

682   Zhang, B., Varney, R. H., Lotko, W., Brambles, O. J., Wang, W., Lei, J., Wiltberger, M., et al.

683   (2015a). Pathways of F region thermospheric mass density enhancement via soft electron

684   precipitation. *Journal of Geophysical Research: Space Physics, 120,* 5824–5831.

685   https://doi.org/10.1002/2015JA020999.

686   Zhang, B., Lotko, W., Brambles, O., Wiltberger, M. & Lyon, J. (2015b). Electron precipita-

687   tion models in global magnetosphere simulations. *Journal of Geophysical Research: Space*

688   *Physics*, *120,* 1035–1056. https://doi.org/10.1002/2014JA020615.

689   Živković T, Buchert S, Ritter P, Palin L, & Opgenoorth, H. (2015). Investigation of energy

690   transport and thermospheric upwelling during quiet magnetospheric and ionospheric condi-

691   tions from the studies of low- and middle-altitude cusp. *Annales Geophysicae*, *33*(6), 623-

692   635. https://doi.org/10.5194/angeo-33-623-2015.

Supporting Information for

Alfvénic Thermospheric Upwelling in a Global Geospace Model

Benjamin Hogan[1,2,†], William Lotko[1,2] and Kevin Pham[2]

[1]Thayer School of Engineering, Dartmouth College, Hanover, NH, USA
[2]High Altitude Observatory, National Center for Atmospheric Research, Boulder, CO, USA
[†]Now at Laboratory for Atmospheric and Space Physics, University of Colorado Boulder, Boulder, CO, USA and
      Department of Aerospace Sciences, University of Colorado Boulder, Boulder, CO, USA

Contents of this file

> Text S1 to S7
> Figures S1 to S5

Introduction

This Supporting Information includes the following sections and figures:

Text S1. CMIT treatment of IMF B_x and **Figure S1** comparing B_x from the OMNI data set with the constrained B_x used in the SIR simulation.

Text S2. CMIT preconditioning.

Text S3. Validity of neglecting neutral gas inertia in collisional Alfvén wave dynamics and **Figure S2** showing the domain of validity for the model ionosphere and thermosphere.

Text S4. Implications of treating the cusp-region geomagnetic magnetic field as straight and uniform and adjustments of model parameters to accommodate this simplification.

Text S5. Illustrative figures of time series of Alfvénic events constrained by CHAMP data (**Figure S3**) and amplitude-frequency spectra of modeled and observed field-aligned current events (**Figure S4**).

Text S6. Altitudes profiles for V, σ_P and σ_0 (**Figure S5**) used to compute FDTD solutions.

Text S7. Notes on Joule and frictional heating.

Text S1. CMIT Treatment of IMF B$_x$

Single point measurements acquired by a solar wind monitor are typically linearly advected in the direction of the solar wind flow, which is very nearly the GSE *x* direction. Consequently, the time variability in IMF B_x implies $\partial B_x / \partial x \neq 0$. Since information on the *y* and *z* dependence of IMF B_y and B_z is not available from single-point upstream measurements, the solenoidal condition, $\nabla \cdot \mathbf{B} = 0$, cannot be maintained without introducing additional constraints on the IMF. We follow the procedure of Wiltberger et al. (2000)[1] and assume the variability in IMF B_x can be represented as

$$B_x(t) = a + bB_y(t) + cB_z(t).$$
(1)

The coefficients *a*, *b*, and *c* are determined by a multiple linear regression fit to all one-minute IMF data samples for the two-day SIR event (60 samples per hour × 48 hours). The fit establishes a plane oriented at a fixed angle relative to the GSE *x* direction with normal direction

$$\vec{\mathbf{n}} = \left(\frac{1}{a}\hat{x} - \frac{b}{a}\hat{y} - \frac{c}{a}\hat{z} \right)$$
(2)

along which the normal magnetic field is constant. This constraint allows a time-dependent B_x to be introduced into the simulation that maintains $\nabla \cdot \mathbf{B} = 0$. For the 26-27 March 2003 event, the fitting procedure gives: $a = Bx_{fit}(0) = 0.99528304$; $b = By_{coef} = -0.24258055$; $c = Bz_{coef} = -0.56645968$. Figure S1 compares B_x from the OMNI dataset with the value used in the CMIT simulation and that calculated from S1.1.
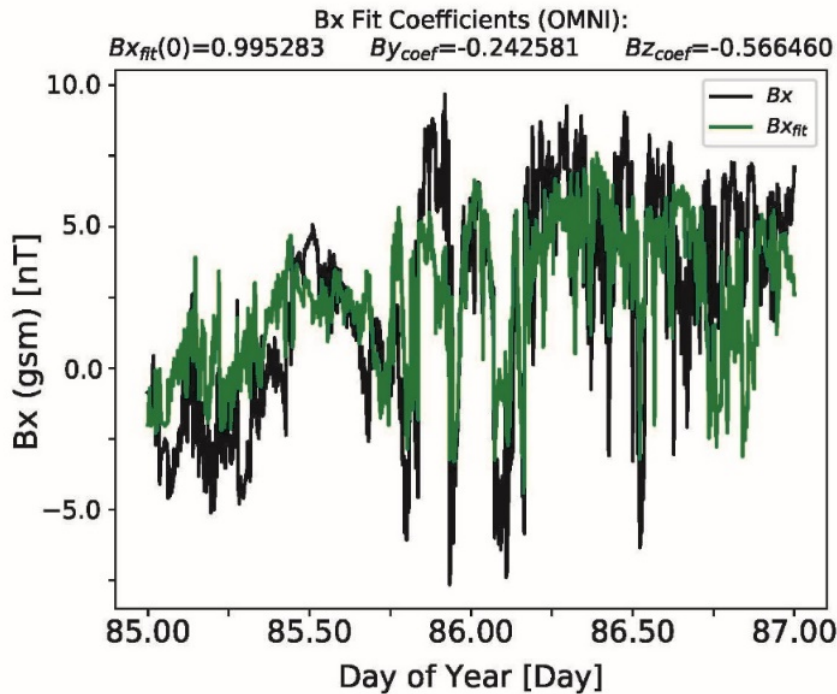

Bx Fit Coefficients (OMNI):
$Bx_{fit}(0)=0.995283$ $By_{coef}=-0.242581$ $Bz_{coef}=-0.566460$

Figure S1. Comparison of measured IMF B_x from the OMNI dataset with the values resulting from the multiple linear regression fit for the 26-27 March 2003.

[1] Wiltberger, M., Pulkkinen, T. I., Lyon, J. G., & Goodrich, C. C. (2000). MHD simulation of the magnetotail during the December 10, 1996, substorm. *Journal of Geophysical Research*, *105*(A12), 27649– 27663, https://doi.org/10.1029/1999JA000251.

Text S2. CMIT preconditioning

CMIT is preconditioned for runs with real-time solar wind inputs as follows. The magnetosphere portion of CMIT, LFM, is typically preconditioned for four hours and fifty minutes before the start of the simulation time (in this study 00 UT March 26 2003).

1. LFM is first initialized with an Earth-centered dipole magnetic field permeating the entire simulation domain, populated by a low density fluid (≈ 0.1 cm^{-3}) composed of protons and alpha particles with number density ratio $n_{He}/n_p = 0.04$.

2. For the first fifty minutes of the LFM preconditioning, the upstream boundary conditions on the IMF and solar wind are specified with a 0 nT IMF, solar wind velocity (V_x, V_y, V_z) = (−400,0,0) km/s, number density $n_{SW} = 5$ cm^{-3} and sound speed $c_{SW} = 40$km/s. As the resulting solar wind dynamic pressure interacts with the dipole magnetic field, it compresses the magnetic cavity on the dayside and stretches the nightside field to form the expected magnetospheric shape. This first phase of initialization prevents the zero-IMF solar wind front from advecting onto a grid cells containing dipole magnetic field lines so the resulting magnetosphere is in the initial low-density, near-vacuum state.

3. At the end of this 50-minute period, the IMF at the upstream boundary is set to (B_x, B_y, B_z) = (0,0,−5) nT for the next two hours with the same solar wind parameters. When the southward IMF contacts the magnetopause, the resulting magnetic reconnection opens the magnetosphere and allows solar wind fluid to enter the magnetosphere.

4. At 2 hours, 50 minutes into the preconditioning, IMF B_z is changed to +5 nT, which produces a quiet state and serves to expand and fully populate the magnetosphere with fluid from the solar wind.

5. The conductances required by MIX during the standalone LFM-MIX preconditioning are calculated from empirical models for precipitation[2] and EUV-induced[3] ionization. These conductances are obtained from TIEGCM after the models are coupled starting at 00 UT 26 March 2003.

CMIT's ionosphere-thermosphere model (TIEGCM) is preconditioned for five days (starting at 00 UT 21 March 2003) before starting the CMIT simulation interval at 00 UT 26 March 2003. For the preconditioning, standalone TIEGCM uses three empirical models as inputs, two of which (high-latitude electric field and electron precipitation models) are changed at 00 UT 26 March 2003 to LMF-MIX inputs. The high-latitude electric field and resulting ionospheric drift velocity during preconditioning are derived from the Kp-parameterized, Heelis empirical model[4]. The extreme ultraviolet (EUV) solar irradiance required by TIEGCM is obtained from the F10.7-parameterized, empirical EUVAC model[5]. TIEGCM uses its default Kp-parameterized, empirical auroral precipitation model during the five-day initialization. TIEGCM retains a history file of Kp and F10.7 values by date, which regulate the empirical models during the five-day preconditioning. EUVAC continues to be regulated by the historical F10.7 during 00 UT 26 March 2003 to 00 UT 28 March 2003.

LFM-MIX and TIEGCM initializations end at 00 UT 26 March 2003, when they are coupled and run as the CMIT model. In CMIT mode, LFM-MIX provides high-latitude convection and electron precipitation

---

[2] Zhang, B., Lotko, W., Brambles, O., Wiltberger, M. & Lyon, J. (2015b). Electron precipitation models in global magnetosphere simulations. Journal of Geophysical Research: Space Physics, 120, 1035–1056. https://doi.org/10.1002/2014JA020615.

[3] Wiltberger, M., Wang, W., Burns, A. G., Solomon, S. C., Lyon, J. G., & Goodrich, C. C. (2004). Initial results from the coupled magnetosphere ionosphere thermosphere model: magnetospheric and ionospheric responses, *Journal of Atmospheric and Solar-Terrestrial Physics, 66*(15-16), 1411-1423. https://doi.org/10.1016/j.jastp.2004.03.026.

[4] Heelis, R. A., Lowell, J. K., & Spiro, R. W. (1982). A model of the high-latitude ionospheric convection pattern. *J. Geophys. Res.*, 87(A8), 6339– 6345. https://doi.org/10.1029/JA087iA08p06339.

[5] Richards, P. G., Fennelly, J. A., & Torr, D. G. (1994). EUVAC: A solar EUV Flux Model for aeronomic calculations. *J. Geophys. Res.*, 99(A5), 8981– 8992. https://doi.org/10.1029/94JA00518.

inputs to TIEGCM, while TIEGCM provides the Pedersen and Hall conductances required by the MIX potential solver. As described in Sec. 2.4, the pre-computed electric field in the Alfvén wave subgrid model is also included in TIEGCM at this time, first with the precomputed value for 26 March 2003, then with the precomputed value for 27 March 2003. When LFM-MIX and TIEGCM are first coupled, immediately after the preconditioning as standalone models, an impulsive change of state occurs in the simulated geospace environment due to discontinuous changes in the conductances used by MIX and the high-latitude convection and precipitation in TIEGCM as well as the addition of Alfvénic Joule heating to TIEGCM. To facilitate relaxation of the impulsive change before the onset of magnetic activity in the SIR event at approximately 1800 UT on 26 March 2003 (cf. Fig. 2) we chose to start running CMIT 18 hours earlier at 00 UT 26 March 2003. This 18-hour buffer period serves to facilitate relaxation of the impulsive change of state in CMIT.

Preconditioning intervals longer than five days for TIEGCM yield modestly different initial states at the end of the preconditioning interval, e.g., differences in neutral density at CHAMP altitudes for twenty-day preconditioning differ from values obtained for five-day preconditioning by less than 20%. Our controlled simulation experiments are concerned primarily with differences in CMIT predictions with and without parameterized Alfvénic heating, so the results of interest are relatively insensitive to moderate differences in IT states obtained from different preconditioning intervals. The buffer interval starting at 00 UT on 26 March 2003 before the onset of intense IMF activity of the SIR event 18 hours later further moderates any sensitivities to preconditioning after 18 UT on 26 March 2003.

Text S3. Validity of neglecting neutral gas inertia in collisional Alfvén wave dynamics

Neutral-gas inertia, mediated by ion-neutral collisions, has been shown to modify Alfvén wave characteristics at sufficiently low wave frequencies and high ion-neutral collision frequencies.[6,7] We derive the conditions of validity that allow this effect to be neglected for the model ionosphere and Alfvén wave spectrum considered in the paper.

The momentum equation for a cold neutral gas with velocity $\mathbf{v}_n$, mass m_n and number density n_n interacting with ion species i with velocity $\mathbf{v}_i$, mass m_i and number density n_i via friction with collision frequency ν_{ni} is

$$n_n m_m \frac{\partial \mathbf{v}_n}{\partial t} = -n_n m_n \nu_{ni} \left(\mathbf{v}_n - \mathbf{v}_i \right) = n_i m_i \nu_{in} \left(\mathbf{v}_i - \mathbf{v}_n \right). \tag{S3.1}$$

The last equality follows from momentum conservation during collisions: $m_n n_n \nu_{ni} = m_i n_i \nu_{in}$. Momentum transfer from electrons is less by a factor of order $m_e \nu_{en} / m_i \nu_{in}$ and has been neglected.

Summing (S3.1) over n, assuming all neutral species have the same wind velocity $\mathbf{u}_n$, gives

$$\rho_n \frac{\partial \mathbf{u}_n}{\partial t} = -\sum_n n_n m_n \nu_{ni} \left(\mathbf{u}_n - \mathbf{v}_i \right) = n_i m_i \nu_i \left(\mathbf{v}_i - \mathbf{u}_n \right) \tag{S3.2}$$

where $\rho_n \equiv \sum_n n_n m_n$ and $\nu_i \equiv \sum_n \nu_{in}$.

Define $\delta_i \equiv n_i m_i / \rho_n$, assume time-harmonic variation, and Fourier Transform (S3.2) with respect to time to obtain the following relationship between Fourier amplitudes (designated as $\tilde{\mathbf{u}}_n$ and $\tilde{\mathbf{v}}_i$):

[6] Hasegawa, Akira & Uberoi, Chanchal (1982). *The Alfven Wave*. DOE critical review Series-Advances in fusion science and engineering, p. 19, Technical Information Center, U.S. Department of Energy. https://www.osti.gov/servlets/purl/5259641.

[7] Song, P., Vasyliūnas, V. M., & Ma, L. (2005). Solar wind-magnetosphere-ionosphere coupling: Neutral atmosphere effects on signal propagation. *J. Geophys. Res., 110*, A09309. https://doi.org/10.1029/2005JA011139.

$$\tilde{\mathbf{u}}_n = \frac{\delta_i \nu_i}{-i\omega + \delta_i \nu_i} \tilde{\mathbf{v}}_i .$$

(S3.3)

The modulus of (S3.3) is

$$\left|\tilde{u}_n\right| = \frac{\delta_i \nu_i}{\sqrt{\omega^2 + \delta_i^2 \nu_i^2}} \left|\tilde{v}_i\right| .$$

(S3.4)

Lysak's (1999)[8] wave equations, from which equations (1)-(3) of Sec. 2.2 are derived, assume the neutrals are effectively stationary $(u_n \ll v_i)$. Equation (S3.4) shows that this assumption is valid when $\omega \gg \delta_i \nu_i$. In this case, the inertia of the neutral gas impedes its response to rapid oscillations in the ion velocity. Then

$$m_i n_i \frac{\partial \mathbf{v}_i}{\partial t} = -m_i n_i \nu_i \left(\mathbf{v}_i - \mathbf{u}_n \right) + e n_i \left(\mathbf{E} + \mathbf{v}_i \times \mathbf{B} \right)$$

$$\approx -m_i n_i \nu_i \mathbf{v}_i + e n_i \left(\mathbf{E} + \mathbf{v}_i \times \mathbf{B} \right).$$

(S3.5)

This approximation is well-satisfied (Fig. S2) for the model ionosphere-thermosphere (described in SI Text S6 and Figure S5) and range of wave frequencies treated in the paper, especially in the lower ionosphere.

Collisional momentum exchange is conserved between ion species and the neutral gas, which is enslaved to the (Alfvénic) oscillating ion gas when $\omega \gg \delta_i \nu_i$: $\rho_n \, \partial \mathbf{u}_n / \partial t \cong n_i m_i \nu_i \mathbf{v}_i$. From this relation and (S3.4) with $\omega \gg \delta_i \nu_i$, we estimate the magnitude of the neutral-gas "quiver" velocity induced by Alfvén-wave ion oscillations as $u_n \sim (\delta_i \nu_i / \omega) v_i$. The maximum Alfvén wave electric field in the cusp is ~ 100 mV/m (cf. Fig. S3) with an implied maximum E×B velocity of ~ 2 km/s. Using the minimum frequency of 0.05 Hz, the factor $\delta_i \nu_i / \omega$ from Fig. S2, is 0.04, 10^{-4}, and 10^{-6} at altitudes of 600 km, 300 km and 150 km, respectively. The maximum quiver velocity in the neutral wind is then ~ 80 m/s near the exobase, ~ 4 m/s in the *F* region, and 0.04 m/s in the *E* region. The average ion velocity encountered by the neutral gas in its transit through the cusp is about 50x less for the example in Fig. S3, and it is less by an additional 10x
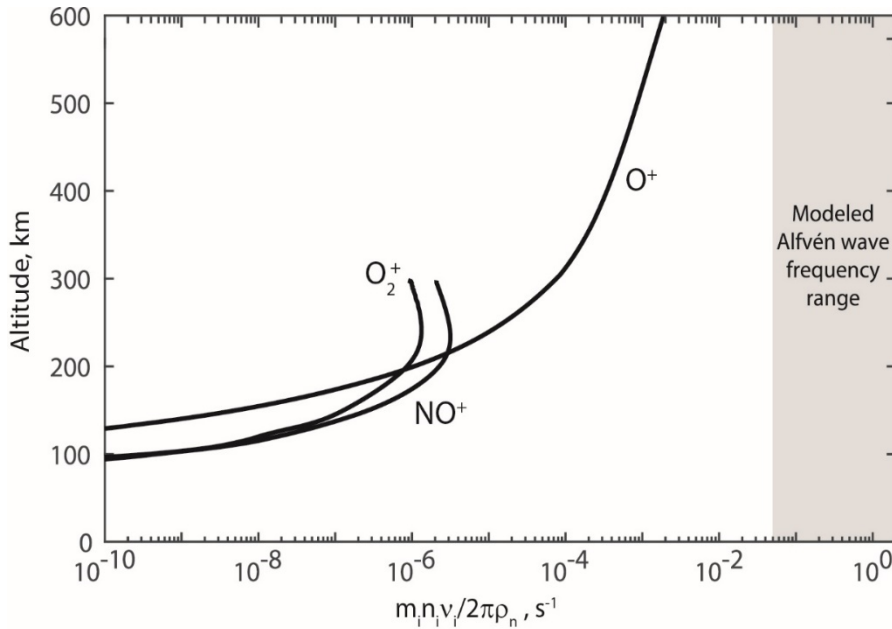

Figure S2. Altitude profile of $m_i n_i \nu_i / 2\pi \rho_n$ for O^+, NO^+, and O_2^+ (dominant ion composition) vs altitude and comparison with the range of Alfvén wave frequencies (gray region, 0.05 Hz to 2 Hz) considered in the paper. Ion and neutral densities and ion-neutral collision frequencies are derived from IRI and MSIS models evaluated in the cusp region for 27 March 2003 (see SI Text S6).

[8] Lysak, R. L. (1999). Propagation of Alfvén waves through the ionosphere: Dependence on ionospheric parameters. *Journal of Geophysical Research, 104*(A5), 10,017–10,030. https://doi.org/10.1029/1999JA900024.

for Alfvén waves with frequencies (> 0.5 Hz), which are most effective in augmenting the Joule heating rate and thermospheric upwelling at F-region altitudes.[9] From these estimates, we conclude that Alfvénic ion forcing of neutral-gas momentum in the cusp is negligible compared to other thermospheric forcings (e.g., frictional quasi-static convection, pressure gradients, advection, etc.).

Text S4. Implications of treating the geomagnetic field as straight and uniform

The actual spatial variation in the background magnetic field[10] introduces the following effects for an Alfvén wave propagating from 1000 km to 90 km altitude at the nominal magnetic latitude (75°) of the cusp: (i) The magnetic field increases by a factor of 1.5, which increases the speed of wave propagation; (ii) the flux tube convergence reduces the perpendicular length scale of the wave structure by a factor of 0.82; and (iii) the field line curvature shifts the geographic location of the magnetic foot point to higher latitude by about 1°. Effect (i) is included in the calculation of the dielectric constant ε in equation (6) and the wave speed V. Effect (ii) tends to reduce the Joule heating rate and increase the Ohmic heating rate, in going from high to low altitude and is modeled as described below. The small effect (iii) influences the interpretation of the geomagnetic latitude of wave energy deposition.

To include effect (ii) in the Alfvén wave solution, we follow Lotko & Zhang (2018)[9] and note that the radial variation of the square of the effective perpendicular wavenumber $k^2(r)$ due to magnetic focusing is $k^2(r) = k_{400}^2 (r_{400}/r)^3 = (2\pi/\lambda_{400})^2 (r_{400}/r)^3$ where k_{400} is the wavenumber specified at 400 km altitude, $r_{400} \equiv 1\,R_E + 400$ km = 6800 km and $r = 1\,R_E + z$ is the radial distance at altitude z. The altitude dependence of the wave solution due to the altitude dependence of the wavenumber may be absorbed into an effective magnetic diffusivity defined as $\eta_{eff}(z) \equiv [r_{400}/(R_E + z)]^3 / \mu_0\,\sigma_0(z)$. With this definition, the solutions for the Alfvén wave electric field are parameterized by the perpendicular wavelength at 400 km altitude.

Text S5. Alfvénic time series and observed and model spectra for FACs

Choosing modal amplitudes of the Alfvén wave electric field at the driver to be

$$E_{m,n}(z_d) = \frac{500 \text{ mV/m}}{n\sqrt{n^2 + 2.4m^2}} \tag{S4.1}$$

yields a peak amplitude for the FAC of approximately 350 μA/m² at 400 km altitude, the mean peak value in Fig.7 of Rother et al. (2007)[11]. A sample time series for the Doppler-derived FAC is shown in Fig. S3, calculated from the Doppler derivative $\partial/V_s \partial t$ of equation (10). Time series for the Alfvén wave electric and magnetic fields, curl-derived FAC (spatial rather than satellite Doppler derivative) and Joule heating rates are also shown in Fig. S3. The amplitude-frequency spectrum from the octave averaged FFT of the FAC in this time series is shown in Fig. S4, superposed on the average spectrum from Fig. 3 of Rother et al. (2007)[11]. The shape of the model spectrum approximates that of observed average spectrum reasonably well at low-frequencies (f < 5 Hz), but it rolls-off more gradually above 5 Hz. The model spectrum at frequencies > 5 Hz is due to Doppler-shift of high wavenumber (k) modes for which the frequency in the spacecraft frame is $f = kV_s$ with $V_s \approx 7.6$ km/s. Ohmic rather than Joule dissipation dominates the absorption in this range (cf. Figs. 2 and 3 of reference[9]). Our results for thermospheric Joule heating are relatively insensitive to this high-k dissipation.

[9] Lotko, W., & Zhang, B. (2018). Alfvénic heating in the cusp ionosphere-thermosphere. *Journal of Geophysical Research: Space Physics, 123*. https://doi.org/10.1029/2018JA025990.

[10] The following analysis is for an Earth-centered dipole field with an equatorial surface value of 3.1×10⁵ T.

[11] Rother, M., Schlegel, K., & Lühr, H. (2007). CHAMP observation of intense kilometer-scale field-aligned currents, evidence for an ionospheric Alfvén resonator. *Annales de Geophysique, 25*(7), 1603–1615. https://doi.org/10.5194/angeo-25-1603-2007.
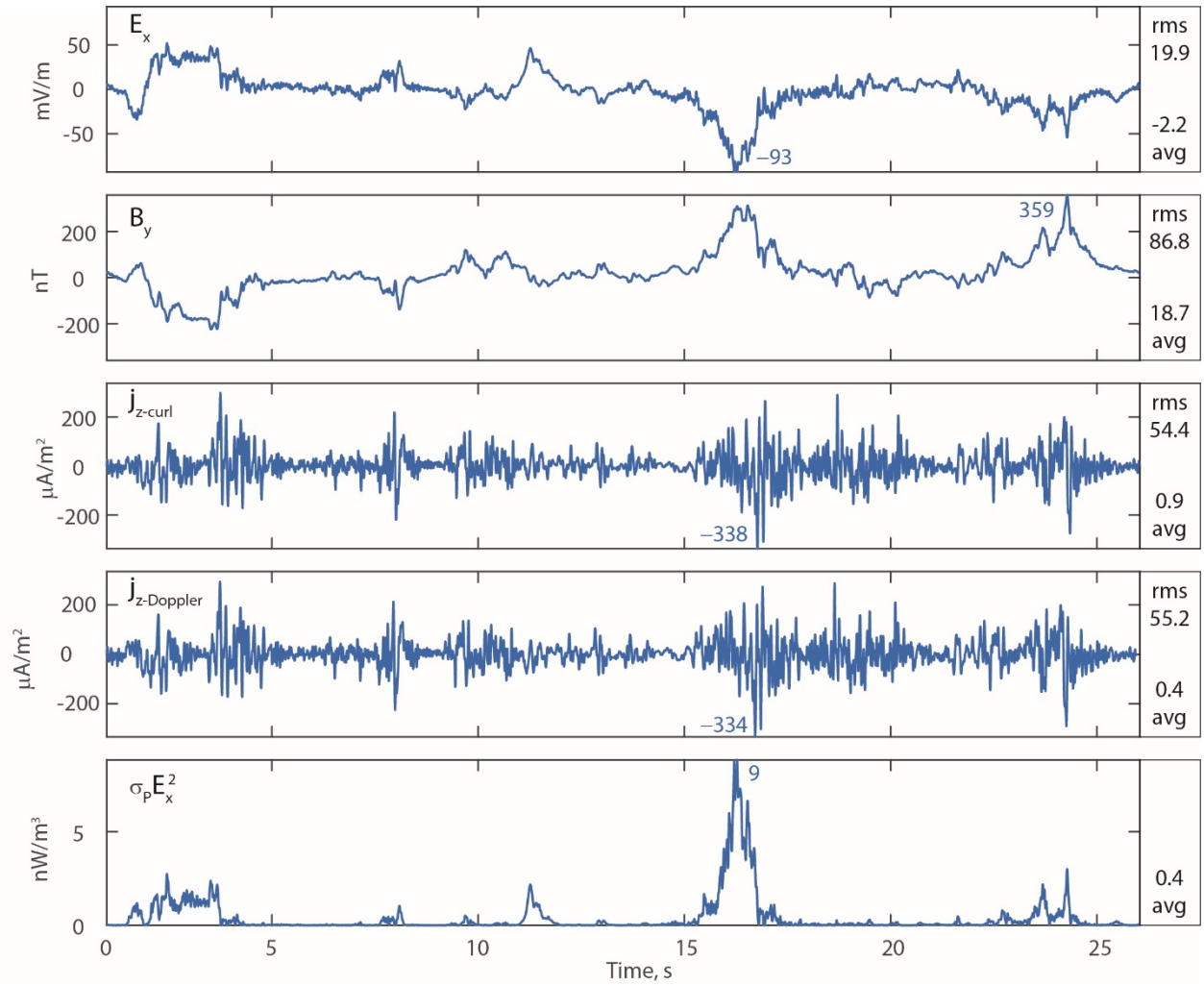
Figure S3. Illustrative synthetic time series of Alfvénic fields along a simulated CHAMP orbital segment through a 200-km wide (MLAT) cusp. The fields are calculated from (9) and (10) with $x = V_s t$. From top to bottom, MLAT component of the electric field E_x, MLT component of the magnetic field B_y, FAC calculated as the curl of B_y, FAC calculated as the Doppler derivative of B_y, and volumetric Joule heating rate $\sigma_P E_x^2$. Maximum value of each field is marked near the peak; rms and average values to the right.
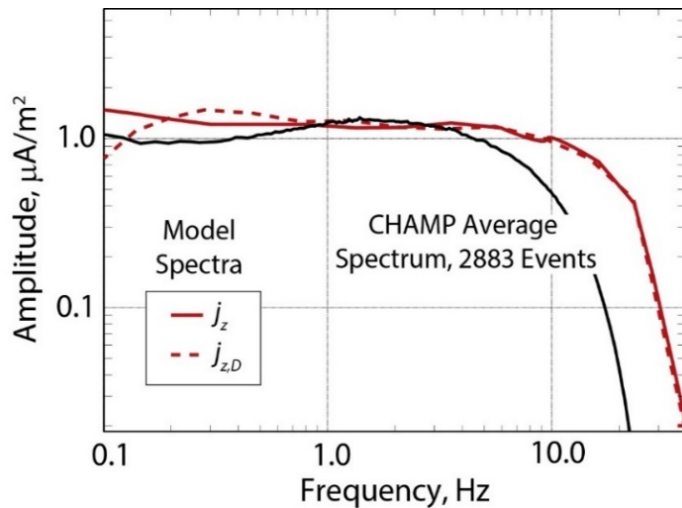
Figure S4. Octave-average spectra for the field-aligned current determined from the curl (j_z) and the Doppler-derivative ($j_{z,D}$) of $B_y(x, z, t)$ for the model ensemble of Alfvén waves and from CHAMP data averaged over 2883 events (Rother et al., 2007)[11]. The model spectra are calculated for average background parameters on 27 March 2003.

Text S6. Altitudes profiles of V, σ_P and σ_0 used to compute FDTD solutions.

      Figure S5 shows profiles for the wave speed V, Pedersen conductivity σ_P, and parallel conductivity σ_0 up to 2000 km altitude on 27 March 2003, calculated using IRI and MSIS to determine the ionospheric and thermospheric variables in equations (4)-(6). These parameters are documented in the repository as "iriday2parameters.txt" and "msisday2parameters.txt." The electron density profile obtained from IRI is subsequently multiplied by a constant so that the peak electron density, or NmF2, matches that of the average electron density profile in the central cusp from the baseline CMIT simulation for each day of the study. These profiles are essentially the same for 26 March 2003. Above 2000 km, V and σ_P are constant and equal to their respective values at 2000 km up to 5000 km. To facilitate convergence of the wave solver, σ_0 is interpolated to a large value specified at the 5000 km top of simulation space, here 10^{10} S/m. The results are not sensitive to this value as long as it is sufficiently large. The resulting profiles are used to calculate FDTD wave solutions as described in section 2.3 of the main text.
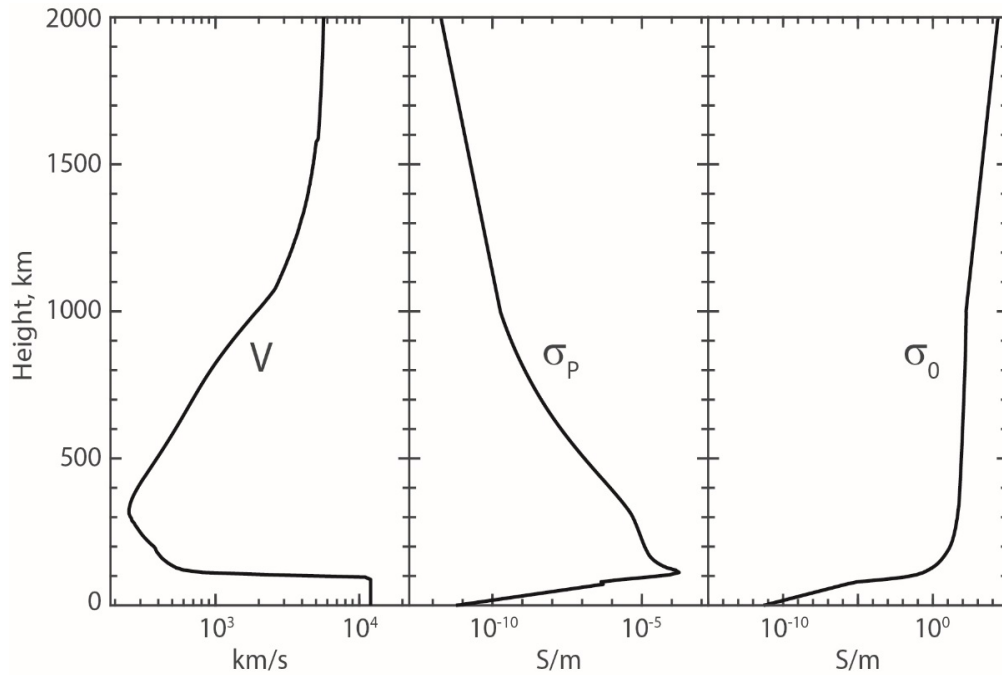

Figure S5. Altitude profiles up to 2000 km for the Alfvén speed (V), Pedersen (σ_P) and parallel (σ_P) conductivities on 27 March 2003 used by the FDTD solver.

Text S7. Notes on electromagnetic energy deposition and frictional heating

      The term Joule heating as conventionally used in the IT literature (and in most of the papers referenced in the Introduction to this paper) refers to the rate of IT electromagnetic energy dissipation calculated as

$$\mathbf{J} \cdot \mathbf{E}' = \sigma_P E_\perp'^2 + \sigma_0 E_\parallel^2 \ . \tag{S7.1}$$

$\mathbf{E}' = \mathbf{E} + \mathbf{u}_n \times \mathbf{B}$ is the electric field in the reference frame of the neutral gas moving with velocity $\mathbf{u}_n$, $\mathbf{B}$ is the background (geomagnetic) field, and σ_P and σ_0 are the Pedersen and direct conductivities given in Sec. 2.2. The contribution $\sigma_0 E_\parallel^2$ to Joule heating is sometimes distinguished as Ohmic heating owing to the functional similarity between σ_0 and the electrical conductivity of a simple solid conductor. In most applications the dominant term in (S7.1) is $\sigma_P E_\perp^2$, which alone is often taken to be the Joule heating rate in IT studies.

Equation (S7.1) assumes the IT variability is quasistatic, i.e., it occurs on time scales much larger than both the gyroperiod and the mean time between collisions. This assumption allows an ionospheric Ohm's law to be expressed as

$$\mathbf{J} = \sigma_P \mathbf{E}'_\perp + \sigma_H \mathbf{b} \times \mathbf{E}' + \sigma_0 E_\parallel \mathbf{b} . \tag{S7.2}$$

From the perspective of kinetic theory, IT Joule and Ohmic heating arise from friction between the electron, ion and neutral gases. When the energy transfer integral for collisional interactions can be given in terms of Maxwell molecule collisions, the heating rate for species r due to collisions with species s with frequency ν_{rs} is[12]

$$\frac{\delta Q_{rs}}{\delta t} = \frac{m_r n_r \nu_{rs}}{m_r + m_s} \left[3 k_b \left(T_s - T_r \right) + m_s \left| \mathbf{v}_r - \mathbf{v}_s \right|^2 \right]. \tag{S7.3}$$

T_s, $\mathbf{v}_s$, m_s and n_s are the species temperature, velocity, atomic mass and number density; k_B is Boltzmann's constant.

At altitudes below 400-500 km, the length scale H for spatial variations and the time scale τ due to ion gyro motion Ω_i^{-1} and ion-neutral collisions ν_{in}^{-1} satisfy $|\mathbf{v}_i - \mathbf{u}_n|\tau \ll H$. In this case, collisional ion-neutral energy exchange achieves an approximate balance between temperature and friction coupling[13] with $3 k_B (T_i - T_n) \cong m_n |\mathbf{v}_i - \mathbf{u}_n|^2$. The heating rate of the neutral gas due to ion friction, $Q_J^{T_n}$ in the notation of Sec. 2.4, is then

$$Q_J^{T_n} = \sum_i \frac{\delta Q_{ni}}{\delta t} \cong \sum_i m_i n_i \nu_{in} \left| \mathbf{v}_i - \mathbf{u}_n \right|^2 . \tag{S7.4}$$

Substituting the ion-neutral velocity difference in the quasi-static limit,

$$\left| \mathbf{v}_i - \mathbf{u}_n \right|^2 = \frac{e^2}{m_i^2} \frac{E'^2}{\Omega_i^2 + \nu_{in}^2} , \tag{S7.5}$$

in (S7.4), the frictional heating rate of the neutral gas can then be equivalently calculated as the Joule heating rate in the neutral-wind frame: [14,15]

$$Q_J^{T_n} = \sum_i m_i n_i \nu_{in} \left| \mathbf{v}_i - \mathbf{u}_n \right|^2 = \sum_i \frac{e^2 n_i}{m_i} \frac{\nu_{in}}{\Omega_i^2 + \nu_{in}^2} E'^2$$
$$= \sum_i \sigma_{Pi} \left| \mathbf{v}_{E \times B} - \mathbf{u}_n \right|^2 = \sigma_P E'^2. \tag{S7.6}$$

The partial Pedersen conductivities σ_{Pi} are defined implicitly by the third equality in (S7.6). This particular form is used to calculate the Joule heating rate (né ion-neutral frictional heating) in the TIEGCM[16].

This result can also be derived in the MHD approximation in the center-of-mass frame for plasma and neutral constituents (essentially the neutral-gas frame),[14] when small corrections for Ohmic heating

[12] Schunk, R., & Nagy, A. (2009). Ionospheres, 2nd Edition, Ch. 4. Cambridge, UK: Cambridge University Press.

[13] Schunk, R. W. (1975). Transport equations for aeronomy. *Planetary and. Space Science, 23*, 437-485. https://doi.org/10.1016/0032-0633(75)90118-X.

[14] St.-Maurice, J.-P., & Schunk, R. W. (1981). Ion-neutral momentum coupling near discrete high-latitude ionospheric features. *J. Geophys. Res., 86*(A13), 11299– 11321. https://doi.org10.1029/JA086iA13p11299.

[15] Thayer, Jeffrey P. & Semeter, Joshua (2004). The convergence of magnetospheric energy flux in the polar atmosphere. *Journal of Atmospheric and Solar-Terrestrial Physics, 66*, 807–824. https://doi.org/10.1016/j.jastp.2004.01.035.

[16] http://www.hao.ucar.edu/modeling/tgcm/doc/description/model_description.pdf

from the generalized Ohm's law and the work done on the neutrals in this frame are neglected.[17,18] Alternatively, the Joule heating rate in the ion reference frame is essentially the Ohmic heating rate in MHD[17,19] except at altitudes from about 120-300 km, where it differs by the additional friction term[18] $n_e m_e v_{en}|\mathbf{u}_{MHD} - \mathbf{u}_n|^2$. Ion-neutral friction appears as separate mechanical energy dissipation in the ion reference-frame formulation and is not associated with electromagnetic energy dissipation in that frame. These formal distinctions regarding neutral gas heating, whether considered as electromagnetic or mechanical energy dissipation, do not change the calculated rate of neutral gas heating or its physical origin arising from the collisional interaction between charged particles and the neutral gas.

In our treatment of Joule dissipation (Sec. 2.4), Ohmic dissipation is unimportant for the perpendicular wavelengths of interest and only conventional Joule dissipation is evaluated for Alfvénic energy deposition $Q_{J,A}$. We now show that (S7.6) can be used to evaluate collisional Alfvénic energy deposition with the result $Q_{J,A} = \sigma_P E_{A\perp}^2$, even though Alfvén wave dynamics do not fully satisfy the quasistatic approximation assumed in deriving (S7.6). This simple Joule heating formula is applicable to Alfvén dynamics because, as discussed in SI Text S3, at sufficiently high wave frequency and low ion-neutral collision frequency, the ratio of the perturbed neutral gas velocity to Alfvén wave ion velocity is negligibly small.

Since Lysak's formulation[8] is the basis for equations (1)-(3) in Sec. 2.2, we start with his equation (A3) for the linear velocity perturbation for ionized species s:

$$\mathbf{v}_{s_\perp} = \frac{e}{m_s \varpi_s^2}\left[\left(\frac{\partial}{\partial t} + \nu_s\right)\mathbf{E}_\perp + \mathbf{E}_\perp \times \mathbf{\Omega}_s\right]. \tag{S7.7}$$

We defined $\varpi_s^2 \equiv \nu_s^2 + \Omega_s^2$. As discussed by Lysak, this expression with $\partial/\partial t \to \omega$ assumes $\omega^2, \omega\nu_s \ll \Omega_s^2$. Retaining corrections with $\omega\nu_s \geq \Omega_s^2$ improves the accuracy of the polarization drift in the E layer (term proportional to $\partial/\partial t$), but the resulting differences in Alfvén wave propagation are minor because the polarization current in the E layer is much less than the Pedersen current.[20] Equation (S7.7) also neglects the small, wave-induced perturbation in neutral velocity stimulated by ion-neutral friction (see SI Text S3). From (S7.7), we obtain

$$v_{s_\perp}^2 = \frac{e^2}{m_s^2 \varpi_s^4}\left|\left(\frac{\partial}{\partial t} + \nu_s\right)\mathbf{E}_\perp + \mathbf{E}_\perp \times \mathbf{\Omega}_i\right|^2 = \frac{e^2}{m_s^2 \varpi_s^4}\left[\left|\frac{\partial \mathbf{E}_\perp}{\partial t}\right|^2 + 2\nu_s \mathbf{E}_\perp \cdot \frac{\partial \mathbf{E}_\perp}{\partial t} + \varpi_s^2 E_\perp^2\right]$$
$$\simeq \frac{\Omega_s^2}{\varpi_s^2}\frac{E_\perp^2}{B_0^2} \tag{S7.8}$$

where $\omega^2, \omega\nu_s \ll \Omega_s^2$ has been used again in the last equality. In light of the analysis in SI Text S3 we can neglect $\mathbf{u}_n$ compared with $\mathbf{v}_i$ in $\mathbf{E}'_\perp$ in (S7.6) to obtain for the Joule heating rate due to Alfvén-wave energy deposition

$$Q_{J,A} \simeq \sum_i m_i n_i \nu_i v_{iA\perp}^2 = \sum_i m_i n_i \nu_i \frac{\Omega_i^2}{\varpi_i^2}\frac{E_{A\perp}^2}{B_0^2} = \sum_i \frac{n_i e^2}{m_i}\frac{\nu_i}{\varpi_i^2}E_{A\perp}^2 = \sigma_P E_{A\perp}^2. \tag{S7.9}$$

[17] Vasyliūnas, V. M., & Song, P. (2005). Meaning of ionospheric Joule heating. *J. Geophys. Res., 110,* A02301, https://doi.org/10.1029/2004JA010615.

[18] Strangeway, R. J. (2012). The equivalence of Joule dissipation and frictional heating in the collisional ionosphere. *J. Geophys. Res., 117,* A02310, https://doi.org/10.1029/2011JA017302.

[19] Gombosi, T. I. (1998). Physics of the Space Environment, Ch, 4. Cambridge, UK: Cambridge University Press.

[20] Sydorenko, D. & Rankin, R. (2017). The stabilizing effect of collision-induced velocity shear on the ionospheric feedback instability in Earth's magnetosphere. *Geophys. Res. Lett., 44,* 6534–6542. https://doi.org/10.1002/2017GL073415.